Supercritical and Subcritical Hopf Bifurcations in a Delay Differential Equation Model of a Heat-Exchanger Tube Under Cross-Flow

Varun Vourganti
Department of Mechanical and Aerospace Engineering,
Indian Institute of Technology Hyderabad,
Kandi,
Sangareddy, Telangana 502285, India

Shanti Swaroop Kandala
Department of Mechanical and Aerospace Engineering,
Indian Institute of Technology Hyderabad,
Kandi,
Sangareddy, Telangana 502285, India

Vamsi C. Meesala
Department of Biomedical Engineering and Mechanics,
Virginia Tech,
495 Old Turner Street, Norris Hall,
Blacksburg, VA 24060

C. P. Vyasarayani[1]
Department of Mechanical and Aerospace Engineering,
Indian Institute of Technology Hyderabad,
Kandi,
Sangareddy, Telangana 502285, India
e-mail: vcprakash@iith.ac.in

Nonlinear vibrations of a heat-exchanger tube modeled as a simply supported Euler–Bernoulli beam under axial load and cross-flow have been studied. The compressive axial loads are a consequence of thermal expansion, and tensile axial loads can be induced by design (prestress). The fluid forces are represented using an added mass, damping, and a time-delayed displacement term. Due to the presence of the time-delayed term, the equation governing the dynamics of the tube becomes a partial delay differential equation (PDDE). Using the modal-expansion procedure, the PDDE is converted into a nonlinear delay differential equation (DDE). The fixed points (zero and buckled equilibria) of the nonlinear DDE are found, and their linear stability is analyzed. It is found that stability can be lost via either supercritical or subcritical Hopf bifurcation. Using Galerkin approximations, the characteristic roots (spectrum) of the DDE are found and reported in the parametric space of fluid velocity and axial load. Furthermore, the stability chart obtained from the Galerkin approximations is compared with the critical curves obtained from analytical calculations. Next, the method of multiple scales (MMS) is used to derive the normal-form equations near the supercritical and subcritical Hopf bifurcation points for both zero and buckled equilibrium configurations. The steady-state amplitude response equation, obtained from the MMS, at Hopf bifurcation points is compared with the numerical solution. The coexistence of multiple limit cycles in the parametric space is found, and has implications in the fatigue life calculations of the heat-exchanger tubes. [DOI: 10.1115/1.4045635]

1 Introduction

In thermal and nuclear power plants, heat exchangers play a vital role in heat transfer between different fluids. In cross-flow heat exchangers, the tubes are susceptible to dynamic fluid forces that cause large-amplitude vibrations. The flow-induced vibrations can potentially damage the tubes and compromise the functionality of the heat exchanger. Thereby, they influence the design parameters that regulate the life span of the heat-exchanger tubes. In nuclear power plants, tube failure can also lead to the mixing of radioactive and nonradioactive fluids, which can be hazardous. Therefore, it is both useful and essential to investigate the stability and vibration behavior of heat-exchanger tubes under cross-flow. Among the different types of excitation mechanisms that lead to tube vibration, fluid elastic instability (FEI) is considered to be the most dangerous as it causes serious damage to the heat-exchanger tubes in just a few hours of operation [1]. It is found that the heat-exchanger tube loses its stability by two mechanisms [2], viz., damping-controlled and stiffness-controlled FEI. In damping-controlled FEI, the net damping in the structure becomes negative due to the positive feedback between the tube and the fluid, leading to large-amplitude vibrations. It has been previously shown that the entire flexible bundle will encounter FEI at the same critical flow velocity, if the negative-damping instability mechanism is the dominant cause for FEI [3,4].

Due to the two-way interaction between the fluid and tube bundles in the heat exchanger, this is a fluid–structure interaction (FSI) problem. Ideally, one must solve the Navier–Stokes equation coupled with the tube deformation to predict the tube response. However, such an exercise is computationally expensive, especially at high Reynolds numbers (Re). Therefore, to investigate the FSI problem with all its complexities, explicit fluid-force models have been developed for predicting FEI in tube-bundles, such as the jet-switching model [5], the quasi-static model [6,7], the semi-analytical model [8], the quasi-steady model [9], the unsteady model [10], the inviscid-flow model [11], and computational fluid dynamics (CFD) models [10]. A drawback of simple theoretical models is that they are known to rely considerably on experimental data for input. Furthermore, even the most accurate of these models like those of Chen [2] and Tanaka and Takahara [10] require unsteady fluid-force data that is extremely difficult to obtain and restricted to certain geometric configurations [12]. CFD models can be very promising, although the computational time and cost of solving the entire FSI problem for a range of flow velocities is immense. Some of these challenges have been documented by Bazilevs et al. [13] and are summarized here. To solve an FSI problem, the differential equations and boundary conditions associated with the fluid and structural domains must be satisfied simultaneously. A robust mesh-moving scheme must be employed. The fluid-domain topology changes as a function of the structural displacement, which must be computed at every time-step. At each time-step, the mesh-moving scheme must guarantee exceptionally high quality and accuracy, which becomes difficult for large structural displacements as in the case of large-amplitude tube vibration. Furthermore, at high Re, a fine enough mesh would be needed to capture the complexity of the

[1]Corresponding author.

Contributed by the Design Engineering Division of ASME for publication in the Journal of Computational and Nonlinear Dynamics. Manuscript received June 11, 2019; final manuscript received November 5, 2019; published online December 19, 2019. Assoc. Editor: Zaihua Wang.

turbulent flow, and a small time-step-size would be needed for convergence.

Owing to the difficulties cited above, the quasi-steady model proposed by Price and Paidoussis [3] has been utilized in this study. Fluid forces are represented using an added mass, damping, and a time-delayed displacement term. The quasi-steady model is essentially the quasi-static model but with the inclusion of a frequency-dependent term arising out of the time-delay due to flow retardation [3]. The quasi-steady model has several advantages. It facilitates analytical calculations that are not possible in CFD studies. It captures some of the most vital characteristics of the FEI problem when the damping-controlled instability mechanism is more dominant, as is the case in this study. In literature, several studies similar to this study serve as precedents for using the quasi-steady model. For predicting FEI, Paidoussis and Li [9] assumed that all the tubes around the tube of interest (flexible tube used for the stability analysis) are rigid. The critical flow velocity at which the single flexible tube encounters FEI was calculated. Paidoussis and Li [9] also studied the chaotic vibrations of a flexible tube subjected to loose supports. Wang and Ni [14] studied the nonlinear dynamics of cantilever tubes subjected to loose supports using the analysis developed by Paidoussis and Li [9], which in turn relies on the quasi-static model of Price and Paidoussis [3]. A similar example is the work by Xia and Wang [15], which explores the postinstability nonlinearity associated with the mean axial extension of a loosely supported flexible cylinder. Wang et al. [16] studied the effect of initial axial load on the instability and nonlinear dynamics of a single flexible tube in an array of rigid cylinders. The quasi-steady theory developed by Price and Paidoussis [3,17] was employed. However, Wang et al. [16] neither studied the spectrum nor rigorously showed the existence of Hopf bifurcations.

The quasi-steady model proposed by Price and Paidoussis [3,17] incorporated a constant time-delay attributed to the retardation of the flow as it approaches the cylinder array. This model has been a precedent for several subsequent time-delay models. Granger and Paidoussis [18] came up with the improved "quasi-unsteady" model that took into account the effect of unsteady forces. Contrary to the flow-retardation effect, a memory function was proposed to model the time-delayed term [19]. Li and Mureithi [19] replaced the time-delay term of the quasi-steady model by the equivalent Theodorsen function. However, their analysis was only suited to low mass-damping parameter values. Mahon and Meskell [20] devised an experimental method to measure the time-delay between tube motion and fluid forces directly by measuring the surface pressure on the cylinder. Results were in qualitative agreement with the time-delay proposed by Price and Paidoussis [17]. Sawadogo and Mureithi [21] determined the time-delay by equating the unsteady fluid forces to the quasi-steady forces. It was found to be of the same order of magnitude as proposed by Price and Paidoussis [17].

Over the past three decades, many researchers have assumed that the heat-exchanger tube to be simply supported. Some examples are found in Refs. [22–24]. As quoted by Paidoussis and Li [9]—"supports in real heat exchangers are somewhere between a simple support and a clamped one, and exact integral relationships between frequencies are rather rare." It should be noted that clamped tubes are stiffer compared to simply supported tubes. Therefore, the stability results for simply supported tubes will be more conservative as compared to fixed tubes. Furthermore, if the tubes are long, and if the support thickness is small as compared to the diameter of the tube, simply supported boundary condition can be assumed.

In this work, the tube is modeled as an Euler–Bernoulli beam with simply supported boundary conditions [16], as explained in Sec. 2. Heat-exchanger tubes undergo thermal expansion, and are consequently subject to thermal loads acting along the axial direction. Further, external tensile loads can be induced by design. The model includes the effect of this axial load (P_0) and nonlinear effects due to large deformations. The quasi-steady model developed by Paidoussis and Li [9] is employed to obtain a partial integro-delay differential equation (DDE) that governs the tube motion. This partial delay differential equation (PDDE) is converted into a single nonlinear DDE using modal truncation, and its linear stability is analyzed in Sec. 3. It should be noted that a DDE is an infinite-dimensional system and therefore, its characteristic equation has infinitely many eigenvalues. Using Galerkin approximations [25,26], the spectrum at different flow velocities and axial loads is obtained in Sec. 3.3. The spectrum contains information on the dominant frequencies (and their damping) that will be present in the transient solution. Dominant eigenvalues from the spectrum are used to generate the stability chart. Furthermore, the normal forms for Hopf bifurcation are derived using the method of multiple scales (MMS) [27] in Sec. 4. These normal forms give insights into the nature of Hopf bifurcation (subcritical or supercritical). The approximate amplitude obtained from the normal-form equations is compared to that from the numerical simulation. From a global bifurcation analysis (Sec. 5), the coexistence of multiple stable and unstable periodic solutions in the parametric space of flow velocity and axial load is shown. Finally, in Sec. 6, the contribution of this work is summarized. The presence of multiple periodic solutions bears significance for fatigue life calculations on the tube. Moreover, as explained later in this paper, tensile axial loads can be induced to control the dynamic response of the tube. Therefore, we expect this study on the tube modeled as a beam to be directly linked to design considerations for heat-exchanger tubes.

2 Mathematical Modeling

Figure 1(*a*) shows the schematic of the heat-exchanger tube bundle with its isometric view along with the coordinate axes. In Fig. 1(*b*), the cross-sectional view of the tube bundle is shown. Figure 1(*c*) shows the idealized model of the heat-exchanger tube as a simply supported beam under axial loads and cross flow fluid forces.

The tube is assumed to be of length L, diameter D, and cross-sectional area A, subjected to cross-flow and axial load P_0, and is modeled in this section using the Euler–Bernoulli beam theory. The governing equation of the transverse displacement $W(x, t)$ of the tube is written as [16]

$$EI\frac{\partial^4 W}{\partial X^4}+C\frac{\partial W}{\partial T}+M\frac{\partial^2 W}{\partial T^2}-\frac{EA}{2L}\frac{\partial^2 W}{\partial X^2}\int_0^L\left(\frac{\partial W}{\partial X}\right)^2 dX+P_0\frac{\partial^2 W}{\partial X^2}=F \tag{1}$$

where EI and C are, respectively, the flexural rigidity and damping coefficient of the tube, X is the spatial coordinate, and T is time. As the beam is simply supported, the boundary conditions are written as $W(0,T)=W(L,T)=0$ and $\partial^2 W/\partial X^2|_{X=0}=\partial^2 W/\partial X^2|_{X=L}=0$. The axial loads P_0 on the tube are a consequence of the applied tensile axial load P_A due to prestress and thermal expansion. Defining α as the thermal expansion coefficient of the heat-exchanger tube material, and $\Delta\theta$ as the temperature differential for the heat-exchanger tube, P_0 can be written as $P_0=EA\alpha\Delta\theta-P_A$. The motion dependent cross-flow-induced forces $F(W,\dot{W},\ddot{W})$ acting on the tube are given by [9]

$$F\left(W,\dot{W},\ddot{W}\right)=-M_f\frac{\partial^2 W}{\partial T^2}-C_f\frac{\partial W}{\partial T}+K_f W(X,T-\Delta T) \tag{2}$$

where

$$M_f=\frac{\pi}{4}\rho D^2 C_{\mathrm{ma}},\quad C_f=\frac{1}{2}\rho\tilde{U}DC_D,\quad K_f=\frac{1}{2}\rho\tilde{U}^2 D\frac{\partial C_L}{\partial W},\quad \text{and}\quad \Delta T=\mu\frac{D}{\tilde{U}} \tag{3}$$

In Eq. (3), ρ and $\tilde{U}$ are, respectively, the density of the fluid and the freestream velocity. C_D, C_L, and C_{ma} are, respectively, the

drag, lift, and added-mass coefficients; μ is a parameter which relates to the tube-array pattern; D is the diameter of the heat-exchanger tube; and ΔT is the time-delay that arises due to the phase lag between cylinder motion and fluid dynamic forces. By introducing the following nondimensional quantities in Eq. (1)

$$w=\frac{W}{D},\quad x=\frac{X}{L},\quad t=\lambda_1^2\sqrt{\frac{EI}{ML^4}}T=\Omega_1 T,\quad \xi=\frac{C}{\Omega_1 M},\quad m=\frac{M}{\rho D^2} \tag{4a}$$

$$U=\frac{2\pi\tilde{U}}{D\Omega_1},\quad p_0=\frac{P_0L^2}{EI},\quad \beta=\frac{\pi C_{\mathrm{ma}}}{\pi C_{\mathrm{ma}}+4m},\quad \text{and}\quad \gamma=\frac{AD^2}{2I\lambda_1^4} \tag{4b}$$

we obtain

$$\frac{1}{1-\beta}\frac{\partial^2 w}{\partial t^2}+\left(\xi+\frac{UC_D}{4\pi m}\right)\frac{\partial w}{\partial t}+\frac{1}{\lambda_1^4}\frac{\partial^4 w}{\partial x^4}+\frac{p_0}{\lambda_1^4}\frac{\partial^2 w}{\partial x^2}-\gamma\frac{\partial^2 w}{\partial x^2}\int_0^1\left(\frac{\partial w}{\partial x}\right)^2 dx-\frac{U^2}{8\pi^2 m}\frac{\partial C_L}{\partial w}w(x,t-\tau)=0 \tag{5}$$

where $\lambda_1=\pi$ is the first nondimensional natural frequency of the tube and the dimensionless time-delay τ is given by $\tau=2\pi/U$, for $\mu=1$ [9]. By considering only the first vibrational mode, the solution $w(x, t)$ of Eq. (5) can be written as

$$w(x,t)=\sqrt{2}\sin(\pi x)q(t) \tag{6}$$

Substituting Eq. (6) into Eq. (5), premultiplying the resulting equation by $\sqrt{2}\sin(\pi x)$, and then integrating with respect to x over the domain $[0, 1]$ results in the following DDE:

$$\frac{1}{1-\beta}\ddot{q}(t)+\left(\xi+\frac{UC_D}{4\pi m}\right)\dot{q}(t)+\left[1-\frac{p_0}{\pi^2}\right]q(t)+\gamma\pi^4 q^3(t)-\frac{U^2}{8\pi^2 m}\frac{\partial C_L}{\partial w}q(t-\tau)=0 \tag{7}$$

Following the procedure outlined in Ref. [16], substituting $\alpha_1=(1-\beta)\xi$, $\alpha_2=((1-\beta)C_D/4\pi m)$, $\alpha_3=(1-\beta)$, $\alpha_4=(1-\beta)\gamma\pi^4$, and $\alpha_5=-((1-\beta)/8\pi^2 m)(\partial C_L/\partial w)$ into Eq. (7), we get

$$\ddot{q}(t)+(\alpha_1+\alpha_2U)\dot{q}(t)+\alpha_3\left[1-\frac{p_0}{\pi^2}\right]q(t)+\alpha_4q^3(t)+\alpha_5U^2q(t-\tau)=0 \tag{8}$$

In Eq. (8), p_0 and U are the parameters of interest, as shall be seen in Sec. 3. It should be noted that the dimensionless time-delay is a derived quantity and is given by $\tau=2\pi/U$. In this paper, the following numerical values are used for the parameters in Eq. (8): $\alpha_1=0.0145$, $\alpha_2=0.00524$, $\alpha_3=0.76$, $\alpha_4=1.1105$, and $\alpha_5=0.026$. These parameters are the same as those used by Wang et al. in Ref. [16].

3 Linear Stability

In this section, the fixed points of Eq. (8) are determined and their linear stability is analyzed. To find the fixed points, we substitute $q(t)=q(t-\tau)=\bar{q}$ into Eq. (8). Next, by dropping the rate-dependent terms at the fixed points, we get

$$\alpha_3\left[1-\frac{p_0}{\pi^2}\right]\bar{q}+\alpha_4\bar{q}^3+\alpha_5U^2\bar{q}=0 \tag{9}$$

Solving for $\bar{q}$ in Eq. (9), we get

$$\bar{q}_1=0,\quad \text{and}\quad \bar{q}_2=\pm\sqrt{\frac{-\alpha_3\left[1-\frac{p_0}{\pi^2}\right]-\alpha_5U^2}{\alpha_4}} \tag{10}$$

In Eq. (10), fixed points $\bar{q}_2$ will be real only if the following condition is satisfied:

$$p_0>\frac{\alpha_5\pi^2U^2+\alpha_3\pi^2}{\alpha_3} \tag{11}$$

To study the stability around these fixed points, we substitute $q(t)=r(t)+\bar{q}$ in Eq. (8), which results in

$$\ddot{r}(t)+(\alpha_1+\alpha_2U)\dot{r}(t)+\alpha_3\left[1-\frac{p_0}{\pi^2}\right]r(t)+3\alpha_4\bar{q}^2r(t)+3\alpha_4\bar{q}r^2(t)+\alpha_4r(t)^3+\alpha_5U^2r(t-\tau)=0 \tag{12}$$

By retaining only the linear terms in Eq. (12), we obtain the following equation:

$$\ddot{r}(t)+(\alpha_1+\alpha_2U)\dot{r}(t)+\alpha_3\left[1-\frac{p_0}{\pi^2}\right]r(t)+3\alpha_4\bar{q}^2r(t)+\alpha_5U^2r(t-\tau)=0 \tag{13}$$

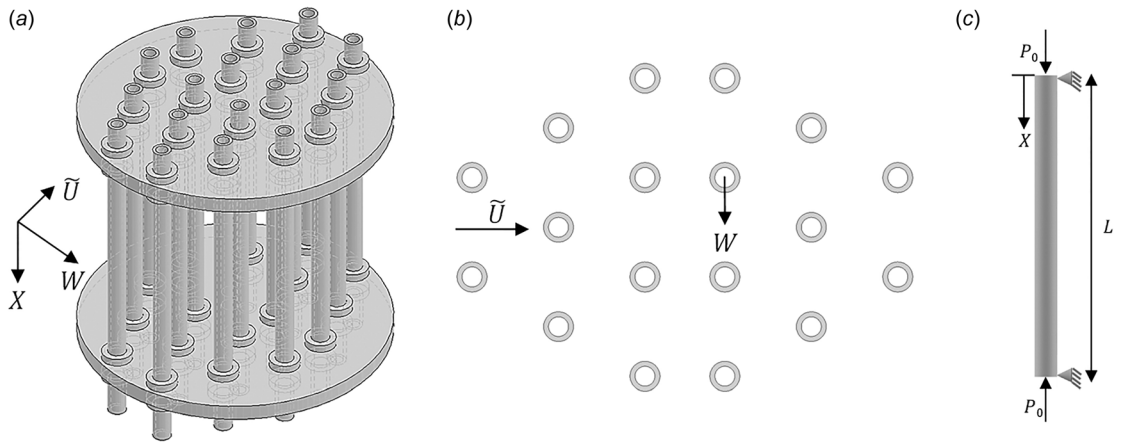

Fig. 1 (*a*) Schematic of the heat-exchanger tube bundle with its isometric view along with the coordinate axes, (*b*) the cross-sectional view of the tube bundle, and (*c*) idealized model of the heat-exchanger tube as a simply supported beam under axial loads and cross flow fluid forces

The stability of Eq. (13) depends on the roots of its characteristic equation. By substituting $r(t) = e^{\lambda t}$ in Eq. (13), we obtain the following characteristic equation:

$$D(\lambda, U, p_0) = \lambda^2 + (\alpha_1 + \alpha_2 U)\lambda + \alpha_3\left[1 - \frac{p_0}{\pi^2}\right] + 3\alpha_4\bar{q}^2 + \alpha_5 U^2 e^{-\lambda\tau} = 0 \tag{14}$$

The above Eq. (14) is a quasi-polynomial (due to the presence of the $e^{-\lambda\tau}$ term) and has infinitely many roots. If the real parts of all the characteristic roots of Eq. (14) are negative, then the equilibrium at $\bar{q}$ is stable. It is generally not possible to obtain the rightmost characteristic roots of Eq. (13) in closed form. However, we can get information about the critical curves that separate the stable and unstable regions in the parametric space of p_0 and U. The stability of Eq. (13) around $\bar{q}$ is lost through Hopf bifurcation when its rightmost characteristic roots cross the imaginary axis (see Fig. 2(*a*)). Alternatively, stability can be lost through a static bifurcation, when the rightmost root crosses the imaginary axis along the real line (see Fig. 2(*b*)). Therefore, to get the stability boundary, we substitute $\lambda = j\omega_{cr}$ and $p_0 = p_{cr}$ in Eq. (14) to obtain the following:

$$\left[-\omega_{cr}^2 + \alpha_3\left(1 - \frac{p_{cr}}{\pi^2}\right) + 3\alpha_4\bar{q}^2 + \alpha_5 U^2\cos(\omega_{cr}\tau)\right] + j\left[(\alpha_1 + \alpha_2 U)\omega_{cr} - \alpha_5 U^2\sin(\omega_{cr}\tau)\right] = 0 \tag{15}$$

Equation (15) will now be used to obtain the critical curves for different equilibrium points.

3.1 Critical Curves for the Equilibrium at $\bar{q}=\bar{q}_1 = 0$.

Substituting $\bar{q} = \bar{q}_1 = 0$ in Eq. (15) and setting the real and imaginary parts to zero, the following equations are obtained:

$$-\omega_{cr}^2 + \alpha_3\left[1 - \frac{p_{cr}}{\pi^2}\right] + \alpha_5 U^2\cos(\omega_{cr}\tau) = 0 \tag{16a}$$

$$(\alpha_1 + \alpha_2 U)\omega_{cr} - \alpha_5 U^2\sin(\omega_{cr}\tau) = 0 \tag{16b}$$

For various values of the axial load p_{cr}, Eqs. (16*a*) and (16*b*) can be solved numerically to determine the variables U and ω_{cr} along the stability boundary. The stability boundary so obtained is represented by curves 1 and 2 in Fig. 3. As discussed earlier, the stability at $\bar{q}_1 = 0$ can also be lost through a static bifurcation (buckling). To determine the critical curve along which the static bifurcation may occur, we substitute $\omega_{cr} = 0$ in Eq. (16*a*). Then, the expression relating p_{cr} and U is obtained as follows:

$$p_{cr} = \frac{\alpha_5\pi^2 U^2 + \alpha_3\pi^2}{\alpha_3} \tag{17}$$

The relationship between p_{cr} and U, given by Eq. (17) with $\omega_{cr} = 0$, is graphically shown by curve 3 in Fig. 3. It should be noted that the equilibrium at $\bar{q}_2$ exists only above curve 3 (see Eq. (11)) in the p_0 and U parameter space.

3.2 Critical Curves for the Equilibrium at $\bar{q} = \bar{q}_2$.

In this section, the stability boundary for equilibrium at $\bar{q}_2$ is discussed. Substituting $\bar{q} = \bar{q}_2$ (Eq. (10)) in Eq. (15), and setting the real and imaginary parts of the resulting expression to zero, we get

$$-\omega_{cr}^2 - 2\alpha_3\left(1 - \frac{p_{cr}}{\pi^2}\right) - 3\alpha_5 U^2 + \alpha_5 U^2\cos(\omega_{cr}\tau) = 0 \tag{18a}$$

$$(\alpha_1 + \alpha_2 U)\omega_{cr} - \alpha_5 U^2\sin(\omega_{cr}\tau) = 0 \tag{18b}$$

For different values of U, one can solve Eqs. (18*a*) and (18*b*) numerically for the values of p_{cr} and ω_{cr} on the stability boundary. This boundary is shown by curves 4 and 5 in Fig. 3. The stability

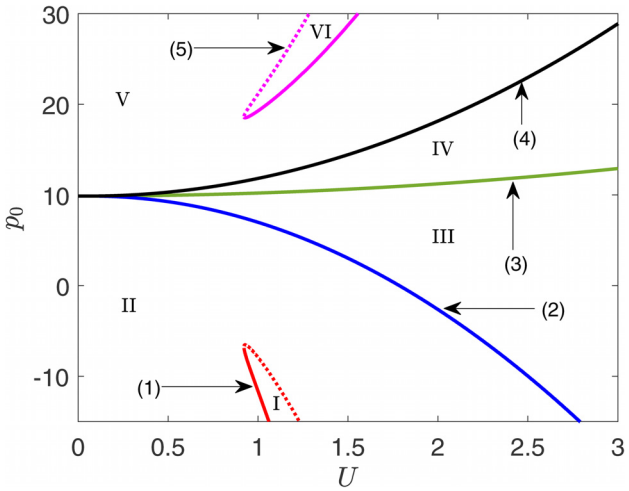

Fig. 3 Critical curves for Hopf and static bifurcation for equilibrium points $\bar{q}_1 = 0$ and $\bar{q}_2$. Curves 1, 2, 4, and 5 correspond to Hopf bifurcation ($\omega_{cr} \neq 0$) and curve 3 corresponds to static bifurcation ($\omega_{cr} = 0$). Six regions are labeled (I–VI) for later discussion.

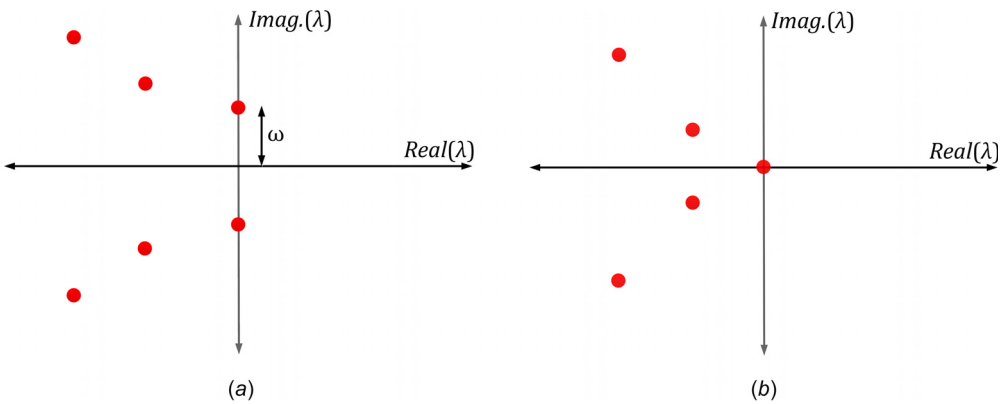

Fig. 2 Two ways in which the rightmost characteristic roots of Eq. (13) can cross the imaginary axis, leading to the loss of stability of equilibrium at $\bar{q}$: (*a*) $\omega_{cr} \neq 0$ (Hopf bifurcation) and (*b*) $\omega_{cr} = 0$ (static bifurcation). It should be noted that in both (*a*) and (*b*), only the first few rightmost roots of the infinite spectrum of the DDE given by Eq. (13) are shown.

of the equilibrium at $\bar{q} = \bar{q}_2$ can also be lost through a static bifurcation (see Fig. 2(*b*)), where $\omega_{cr} = 0$. Substituting $\omega_{cr} = 0$ in Eq. (18*a*), the equation relating p_{cr} and U is obtained as follows:

$$p_{cr} = \frac{\alpha_5 \pi^2 U^2 + \alpha_3 \pi^2}{\alpha_3} \tag{19}$$

Equation (19) is the same as Eq. (17) and hence the stability boundary is given by curve 3 in Fig. 3. In Fig. 3, all the stability boundaries are shown. However, one must exercise caution when determining the stable and unstable regions from Fig. 3. For example, the conditions for Hopf bifurcation given by Eqs. (16*a*) and (16*b*) or by Eqs. (18*a*) and (18*b*) are satisfied as long as a pair of roots lies on the imaginary axis. In Fig. 4(*a*), although the system is unstable, the second pair of eigenvalues lies exactly on the imaginary axis and satisfies the analytical conditions imposed on the stability boundary. Similarly, the condition $\omega_{cr} = 0$, imposed on the characteristic roots for the case of static bifurcation, is satisfied even for the case shown in Fig. 4(*b*) for which the system is unstable. Therefore, it is difficult to determine the stable and unstable regions directly from Fig. 3. For understanding the stability behavior of the tube, we divide the stability chart into six regions, shown as I–VI in Fig. 3. In Sec. 3.3, we shall develop Galerkin approximations for the linear DDE given by Eq. (13) and numerically obtain its characteristic roots, after which it is straightforward to comment on stability. The distribution of the characteristic roots (spectrum) of Eq. (13) for different flow velocities and axial loads will also be studied. The spectrum will also give us insights into the regions of maximum damping in the p_0 and U space.

3.3 Spectrum. Several methods exist in the literature to study the stability of time-delayed systems by obtaining their characteristic roots. Some of these methods are Lambert W function [28–31], Galerkin approximations [32–34], semidiscretization [35], pseudospectral collocation [36–38], continuous-time approximation [39,40], and quasi-polynomial root finder algorithm (QPmR) [41]. Cluster treatment of characteristic roots approach is another powerful tool to obtain accurate stability charts for time-delayed systems [42]. Pekař and Gao have recently presented an exhaustive list of various methods to study the stability of DDEs [43]. In this section, using a Galerkin method [25,26], we derive an ODE-based approximation for Eq. (13), thereby converting the DDE into a finite dimensional ODE system. Equation (13) is converted into the following form:

$$\ddot{r}(t) + A_1 \dot{r}(t) + A_2 r(t) + A_3 r(t-\tau) = 0 \tag{20}$$

The procedure for converting a DDE into a system of ODEs has already been reported in the literature [25,26]; however, the procedure is repeated here for completeness. By defining the state variables $\mathbf{r}(t) = [r(t),\ \dot{r}(t)]^{\mathrm{T}}$ in Eq. (20), we get

$$\dot{\mathbf{r}}(t) = \mathbf{A}\mathbf{r}(t) + \mathbf{B}\mathbf{r}(t-\tau) \tag{21}$$

In Eq. (21), the following time-shift transformation is introduced:

$$\mathbf{r}(t+s) = \mathbf{y}(s,t) \tag{22}$$

Differentiating Eq. (22) with respect to s and t, and using the chain rule, we obtain

$$\frac{\partial \mathbf{y}(s,t)}{\partial t} = \frac{\partial \mathbf{y}(s,t)}{\partial s}, \quad -\tau \le s \le 0 \tag{23}$$

From Eq. (22), we have $\mathbf{r}(t) = \mathbf{y}(0,t)$ and $\mathbf{r}(t-\tau) = \mathbf{y}(-\tau,t)$. Substituting these relations in Eq. (21), we get

$$\left.\frac{\partial \mathbf{y}(s,t)}{\partial t}\right|_{s=0} = \mathbf{A}\mathbf{y}(0,t) + \mathbf{B}\mathbf{y}(-\tau,t) \tag{24}$$

In essence, we have converted the DDE given by Eq. (20) into an equivalent PDE (Eq. (23)) and its boundary condition (Eq. (24)). Now, we approximate the solution of Eq. (23) as follows:

$$y_i(s,t) = \sum_{j=1}^{N} \psi_j(s) z_{ij}(t) = \boldsymbol{\psi}(s)^{\mathrm{T}} \mathbf{z}_i(t), \quad i = 1,2 \tag{25}$$

Here, $\boldsymbol{\psi}(s) = [\psi_1(s),\ \psi_2(s),\ \ldots,\ \psi_N(s)]^{\mathrm{T}}$ are the basis functions and $\mathbf{z}_i(t) = [z_{i1}(t),\ z_{i2}(t), \ldots, z_{iN}(t)]^{\mathrm{T}}$ are the independent coordinates. By defining $\boldsymbol{\Psi}(s) \in \mathbb{R}^{2N\times 2}$ and $\boldsymbol{\beta}(t) \in \mathbb{R}^{2N\times 1}$ as follows:

$$\boldsymbol{\Psi}(s) = \begin{bmatrix} \boldsymbol{\psi}(s) & 0 \\ 0 & \boldsymbol{\psi}(s) \end{bmatrix}, \quad \boldsymbol{\beta}(t) = \left[\mathbf{z}_1^{\mathrm{T}}(t),\ \mathbf{z}_2^{\mathrm{T}}(t)\right]^{\mathrm{T}} \tag{26}$$

Equation (25) can be written as

$$\mathbf{y}(s,t) = \left[\boldsymbol{\psi}^{\mathrm{T}}(s)\mathbf{z}_1(t), \boldsymbol{\psi}^{\mathrm{T}}(s)\mathbf{z}_2(t)\right]^{\mathrm{T}} = \boldsymbol{\Psi}^{\mathrm{T}}(s)\boldsymbol{\beta}(t) \tag{27}$$

Substituting Eq. (27) into Eq. (23), we get

$$\boldsymbol{\Psi}^{\mathrm{T}}(s)\dot{\boldsymbol{\beta}}(t) = \boldsymbol{\Psi}'(s)^{\mathrm{T}}\boldsymbol{\beta}(t) \tag{28}$$

where $\boldsymbol{\Psi}'(s)$ is the derivative of $\boldsymbol{\Psi}(s)$ with respect to s. Premultiplying Eq. (28) by $\Psi(s)$ and integrating with respect to s over the domain $[-\tau, 0]$, we obtain the following:

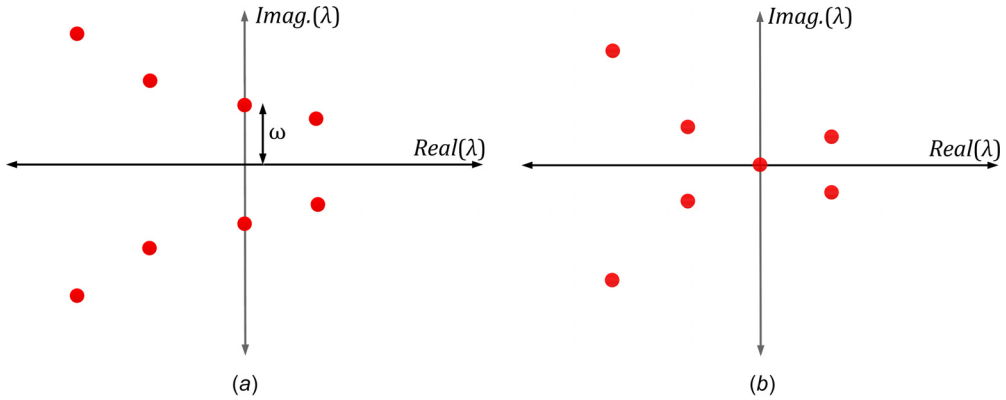

Fig. 4 Possible locations of the characteristic roots on the critical curves for the case of (*a*) $\omega_{cr} \neq 0$ and (*b*) $\omega_{cr} = 0$. It should be noted that in both (*a*) and (*b*), only the first few rightmost roots of the infinite spectrum of the DDE given by Eq. (13) are shown.

$$\left(\int_{-\tau}^{0}\boldsymbol{\Psi}(s)\boldsymbol{\Psi}^{\mathrm{T}}(s)ds\right)\dot{\boldsymbol{\beta}}(t)=\left(\int_{-\tau}^{0}\boldsymbol{\Psi}(s)\boldsymbol{\Psi}'(s)^{\mathrm{T}}ds\right)\boldsymbol{\beta}(t) \tag{29}$$

Equation (29) can be rewritten as

$$\mathbf{C}\dot{\boldsymbol{\beta}}(t)=\mathbf{D}\boldsymbol{\beta}(t) \tag{30}$$

where $\mathbf{C}$ and $\mathbf{D}$ are square, block-diagonal matrices of dimension $2N$, given by

$$\mathbf{C}=\begin{bmatrix}\mathbf{C}^{(1)} & 0\\ 0 & \mathbf{C}^{(2)}\end{bmatrix}^{\mathrm{T}},\quad \mathbf{D}=\begin{bmatrix}\mathbf{D}^{(1)} & 0\\ 0 & \mathbf{D}^{(2)}\end{bmatrix}^{\mathrm{T}} \tag{31}$$

Submatrices $\mathbf{C}^{(i)}$ and $\mathbf{D}^{(i)}$ are defined as follows:

$$\mathbf{C}^{(i)}\triangleq\int_{-\tau}^{0}\boldsymbol{\psi}_i(s)\boldsymbol{\psi}_i^{\mathrm{T}}(s)ds,\quad \mathbf{D}^{(i)}\triangleq\int_{-\tau}^{0}\boldsymbol{\psi}_i(s)\boldsymbol{\psi}_i'(s)^{\mathrm{T}}ds,\quad i=1,2 \tag{32}$$

The matrix of boundary conditions, of dimension $2\times 2N$, can be derived by substituting Eq. (27) into Eq. (24) as follows:

$$\boldsymbol{\Psi}^{\mathrm{T}}(0)\dot{\boldsymbol{\beta}}(t)=\left[\mathbf{A}\boldsymbol{\Psi}^{\mathrm{T}}(0)+\mathbf{B}\boldsymbol{\Psi}^{\mathrm{T}}(-\tau)\right]\boldsymbol{\beta}(t) \tag{33}$$

Equations (30) and (33) can be combined as follows:

$$\mathbf{M}\dot{\boldsymbol{\beta}}(t)=\mathbf{K}\boldsymbol{\beta}(t) \tag{34}$$

Matrices $\mathbf{M}$ and $\mathbf{K}$ are of dimension $2N\times 2N$, and are obtained by replacing the Nth and $2N$th rows of Eq. (30) with the first and second rows of Eq. (33), respectively. Defining $\mathbf{G}\triangleq\mathbf{M}^{-1}\mathbf{K}$, Eq. (34) can be written as follows:

$$\dot{\boldsymbol{\beta}}(t)=\mathbf{G}\boldsymbol{\beta}(t) \tag{35}$$

The system of ODEs given by Eq. (35) approximates the DDE given by Eq. (20), and the eigenvalues $(\hat{\lambda}_i)$ of $\mathbf{G}$ approximate the characteristic roots of Eq. (14). As N is increased, the eigenvalues of $\mathbf{G}$ converge to the rightmost characteristic roots of Eq. (14) [25,26]. The error E_i, $\forall i=\{1,2,\ldots,2N\}$, is defined as the absolute value of $D(\hat{\lambda}_i)$ (Eq. (14)), obtained by substituting the eigenvalues of $\mathbf{G}$ into Eq. (14). All $\hat{\lambda}_i$ for which $E_i<10^{-4}$ are considered to be converged to the characteristic roots of Eq. (14). In this work, shifted Legendre polynomials are used to approximate the solution (Eq. (25)) and are defined as follows:

$$\psi_1(s)=1 \tag{36a}$$

$$\psi_2(s)=1+\frac{2s}{\tau} \tag{36b}$$

$$\psi_k(s)=\frac{(2k-3)\psi_2(s)\psi_{k-1}(s)-(k-2)\psi_{k-2}(s)}{k-1},\quad k=3,4,\ldots,N \tag{36c}$$

In the literature, it is reported that shifted Legendre polynomials have shown good convergence properties [26]. The entries of matrices $\mathbf{C}^{(p)}$ and $\mathbf{D}^{(p)}$ can be expressed in closed form as follows:

$$\mathbf{C}_{ij}^{(p)}=\begin{cases}\dfrac{\tau}{2i-1}, & \text{if } i=j\\ 0, & \text{otherwise}\end{cases},\qquad \mathbf{D}_{ij}^{(p)}=\begin{cases}2, & \text{if } i<j \text{ and } i+j \text{ is odd}\\ 0, & \text{otherwise}\end{cases},\quad p=1,2 \tag{37}$$

where $i=1,2,\ldots,N$ and $j=1,2,\ldots,N$. If we consider N terms in the series solution given by Eq. (25), approximately $N/2$ eigenvalues of matrix $\mathbf{G}$ converge to the rightmost roots of the characteristic polynomial (Eq. (14)). In this paper, we use $N=100$ and this value of N was found to be sufficient for generating an accurate stability chart for Eq. (20).

Figure 5 shows the stability chart for Eq. (14) in the $[U, p_0]$ plane, obtained using the Galerkin approximation method. To generate the stability chart, the region of Fig. 5 has been discretized into 300×4500 points. At each of these points, the eigenvalues of matrix $\mathbf{G}$ (see Eq. (35)) are evaluated. If all the eigenvalues fall on the left half of complex plane, the system is considered to be stable; otherwise, it is considered unstable. All the white regions shown in Fig. 5 (i.e., I, III, IV, and VI) are unstable. The color contours in Fig. 5 indicate the damping present in the rightmost root in the stable region. It should be noted that for a retarded delay differential equation, the decay rate will depend on the real parts of all the infinite roots. However, the contribution to the solution from the rightmost root is the highest and is the last to decay. Therefore, we have assumed the real part of rightmost root to be the damping in the system. The highest damping (λ furthest into the left half-plane) is present around $U=2.34$ and for $p_0=30$. Figure 5 must be contrasted with Fig. 3 as the boundary curves shown in these figures are same. From the stability chart, we can conclude that the zero equilibrium ($\bar{q}=\bar{q}_1=0$) is stable only in region II. The buckled equilibrium at $\bar{q}=\bar{q}_2$ exists in regions IV, V, and VI, but it is stable only in region V. An important observation from the stability chart is that curve 3, which separates regions III and IV, does not represent the critical curve for static bifurcation since the system is unstable in both regions III and IV.

As discussed in Sec. 2, for a given flow velocity, from the stability chart, the axial tension P_A can be adjusted for maximum damping. For example, if the heat exchanger is operated at $U=2$, the induced axial load can be selected to $p_0=-15$ for optimal damping of vibrations. It should be noted that with $p_0=-15$, the beam settles at zero equilibrium.

Now, we study the distribution of the characteristic roots for different critical points in Fig. 5 along $U=1$, shown by the dashed vertical line. Points P_1, P_2, and P_3 in Fig. 5 are the bifurcation points of zero equilibrium. Similarly, P_5, P_6, and P_7 are the bifurcation points of buckled equilibrium. The value of critical axial load p_{cr} and frequency ω_{cr} at these points is shown in the second and third columns of Table 1, respectively.

Figures 6(*a*)–6(*f*) show the 12 rightmost characteristic roots of Eq. (14) corresponding to points P_1, P_2, P_3, P_5, P_6, and P_7. It can be seen from Figs. 6(*a*)–6(*f*) that the rightmost roots are purely

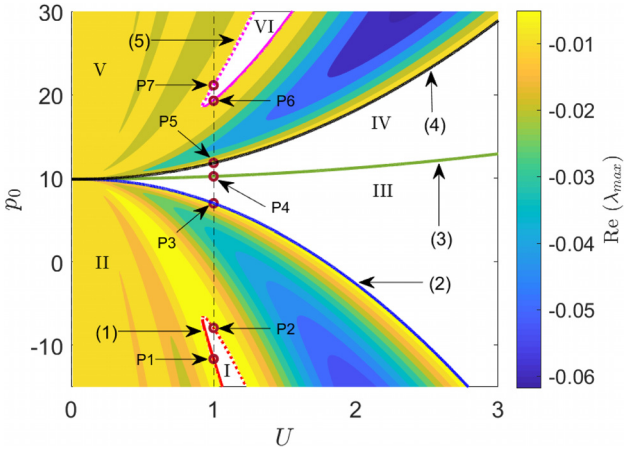

Fig. 5 Stability chart in the $[U, p_0]$ plane, generated using the Galerkin approximation method, with $N=100$. Color contours indicate the damping present in the rightmost root.

imaginary indicating the possibility of Hopf bifurcation. In Fig. 7, the spectrum corresponding to point P_4 is shown. It can be seen that there is a characteristic root at the origin, which is expected as this point falls on curve 3 in Fig. 5. However, the system is already unstable (see Fig. 7). Therefore, P_4 is not a bifurcation point.

In Fig. 8, we show the real part of the rightmost root in the region $-15 \le p_0 \le 10.207$ for the zero equilibrium ($\bar{q} = \bar{q}_1 = 0$), represented by the red line. The blue dotted line shows the real part of the rightmost root in the region $10.207 \le p_0 \le 30$ for the buckled equilibrium ($\bar{q} = \bar{q}_2$). We can clearly see from Fig. 8 that the real part of the rightmost root crosses the imaginary axis at points P_1, P_2, P_3, P_5, P_6, and P_7 with nonzero slope $(\bar{\Gamma})$ with respect to the parameter p_0. This clearly indicates the presence of a Hopf bifurcation. The value of $\bar{\Gamma} = \text{Real}(d\lambda/dp_0)|_{p_0=p_{cr}} \approx \text{Real}\left(\lambda|_{(p_{cr}+\sigma)} - \lambda|_{(p_{cr}-\sigma)}/2\sigma\right)$ at these points is shown in the fourth column of Table 1.

4 Hopf Bifurcation

In this section, the Hopf bifurcation of Eq. (12) is studied. Equation (12) is rewritten here for reference

$$\ddot{r}(t) + (\alpha_1 + \alpha_2 U)\dot{r}(t) + \alpha_3\left[1 - \frac{p_0}{\pi^2}\right] r(t) + 3\alpha_4\bar{q}^2 r(t) + 3\alpha_4\bar{q}r^2(t) + \alpha_4 r(t)^3 + \alpha_5 U^2 r(t-\tau) = 0 \tag{38}$$

From the stability chart (see Fig. 5), we can see that by fixing U (at 1) and increasing p_0, the stability of the equilibrium at $r = 0$ switches when we cross curves 1 and 2. It should be noted that curves 1 and 2 in the stability chart correspond to the stability boundary for $\bar{q} = \bar{q}_1 = 0$ in Eq. (12). Similarly, for a fixed value of U, the stability of the equilibrium at $r = 0$ switches when we cross curves 4 and 5 in the stability chart. It should be noted that curves 4 and 5 in the stability chart correspond to the stability boundary for $\bar{q} = \bar{q}_2$, i.e., for the buckled equilibrium case of Eq. (12). In order to determine the nature of Hopf bifurcation (supercritical or subcritical), one must obtain the normal forms of Eq. (38) at the Hopf bifurcation points. The normal forms near the Hopf bifurcation can be obtained using the MMS [27] or the method of averaging [44,45] or center manifold reduction [46]. These normal forms can be used to study the stability of the limit cycles born out of Hopf bifurcation. In this section, the normal-form equations are obtained using the MMS.

4.1 Hopf Bifurcation for the Case of $\bar{q} = \bar{q}_1 = 0$. Substituting $\bar{q} = \bar{q}_1 = 0$ into Eq. (38), we get

$$\ddot{r}(t) + (\alpha_1 + \alpha_2 U)\dot{r}(t) + \alpha_3\left[1 - \frac{p_0}{\pi^2}\right] r(t) + \alpha_4 r(t)^3 + \alpha_5 U^2 r(t-\tau) = 0 \tag{39}$$

Table 1 Values of p_{cr}, ω_{cr}, $\bar{\Gamma}$ (numerical), Γ (analytical), and relative error between the latter ($(\bar{\Gamma}-\Gamma)/\Gamma$) expressed as a percentage, for different bifurcation points as shown in the stability chart (see Fig. 5)

Point	p_{cr}	ω_{cr}	$\bar{\Gamma}$ ($\times 10^{-4}$)	Γ ($\times 10^{-4}$)	Relative error (%)
P_1	−11.652	1.285	5.7416	5.7274	0.2479
P_2	−7.923	1.175	−6.6533	−6.6375	0.2380
P_3	6.978	0.445	144.5214	144.5937	0.0500
P_5	11.822	0.445	−289.5746	−288.7426	0.2881
P_6	19.273	1.175	13.2800	13.2417	0.2892
P_7	21.137	1.285	−11.3442	−11.3089	0.3121

The following parameters are now introduced into Eq. (39):

$$2\zeta = \alpha_1 + \alpha_2 U, \quad k_1 = \alpha_3, \quad k_2 = \frac{\alpha_3}{\pi^2}, \quad k_4 = \alpha_5 U^2 \tag{40}$$

Equation (39) now becomes

$$\ddot{r}(t) + 2\zeta\dot{r}(t) + k_1 r(t) - k_2 p_0 r(t) + \alpha_4 r^3(t) + k_4 r(t-\tau) = 0 \tag{41}$$

Dropping the nonlinear term in Eq. (41) and introducing the parameters ζ, k_1, k_2, and k_4 (Eq. (40)) into the characteristic equation of the linearized problem, we have

$$D(\lambda, p_0) \equiv \lambda^2 + 2\zeta\lambda + k_1 - k_2 p_0 + \frac{k_4}{e^{\lambda\tau}} = 0 \tag{42}$$

where λ is an implicit function of p_0. From the chain rule of differentiation, we have

$$\frac{dD}{dp_0} = \frac{\partial D}{\partial p_0} + \frac{\partial D}{\partial \lambda}\frac{d\lambda}{dp_0} = 0 \tag{43}$$

Solving Eq. (43) for $(d\lambda/dp_0)$, we get

$$\frac{d\lambda}{dp_0} = -\frac{\partial D}{\partial p_0}\left(\frac{\partial D}{\partial \lambda}\right)^{-1} = \frac{k_2}{2\lambda + 2\zeta - k_4 e^{-\lambda\tau}\tau} \tag{44}$$

At a Hopf bifurcation, we have to show that $\Gamma = \text{Real}(d\lambda/dp_0)|_{p_0=p_{cr},\lambda=j\omega_{cr}} \neq 0$. Substituting $p_0 = p_{cr}$ and $\lambda = j\omega_{cr}$ in Eq. (44) and using the identity $e^{-j\omega_{cr}\tau} = \cos(\omega_{cr}\tau) - j\sin(\omega_{cr}\tau)$, we get

$$\Gamma = \frac{k_2\left(-2\zeta + k_4\tau\cos(\omega_{cr}\tau)\right)}{-4\zeta^2 + 4\zeta k_4\tau\cos(\omega_{cr}\tau) - k_4^2\tau^2 - 4\omega_{cr}^2 - 4\omega k_4\tau\sin(\omega_{cr}\tau)} \tag{45}$$

Substituting $\sin(\omega_{cr}\tau)$ and $\cos(\omega_{cr}\tau)$ obtained from Eqs. (16*a*) and (16*b*) in Eq. (45), we get

$$\Gamma = \frac{k_2\left(2\zeta - \tau\omega_{cr}^2 + \tau k_1 - \tau k_2 p_{cr}\right)}{4(\zeta\tau + 1)\omega_{cr}^2 + 4\zeta^2 + 4\zeta\tau k_1 - 4\zeta\tau k_2 p_{cr} + k_4^2\tau^2} \tag{46}$$

It can be seen from Table 1 that the analytically predicted values of Γ (velocity of root crossing) at the Hopf bifurcation points are in close agreement with those obtained numerically from Galerkin approximations. At points P_1, P_2, and P_3, we have $\Gamma \neq 0$. This guarantees the occurrence of the Hopf bifurcation at these points. It should be noted that $\Gamma > 0$ indicates the crossing of purely imaginary roots from left to right (stable to unstable) in the complex plane. Conversely, $\Gamma < 0$ indicates the crossing of purely imaginary roots from right to left (unstable to stable) in the complex plane.

As the focus of this section is to study the motion around the Hopf bifurcation points, we perturb the parameter p_0 using a detuning parameter Δ. Substituting $p_0 = p_{cr} + \epsilon\Delta$, $\kappa = k_1 - k_2 p_{cr}$, and $k_3 = \alpha_4/\epsilon$ in Eq. (41), we get

$$\ddot{r}(t) + 2\zeta\dot{r}(t) + \kappa r(t) + k_4 r(t-\tau) + \epsilon\left[k_3 r^3(t) - k_2\Delta r(t)\right] = 0 \tag{47}$$

Using the MMS for DDEs as proposed by Das and Chatterjee [27], the solution $r(t)$ of Eq. (47) is expanded as follows:

$$r(t) = r(t, T_0) = r_0(t, T_0) + \epsilon r_1(t, T_0) + \cdots \tag{48}$$

In Eq. (48), $t = \epsilon^0 t$ is the actual time-scale, and $T_0 = \epsilon^1 t$ is the slow time-scale. The time-delay term $r(t-\tau)$ is expanded as follows:

$$r(t-\tau) = r_0(t-\tau, T_0) + \epsilon\left(r_1(t-\tau, T_0) - \tau\frac{\partial r_0(t-\tau, T_0)}{\partial T_0}\right) + \cdots \tag{49}$$

Upon substituting Eqs. (48) and (49) into Eq. (47), the terms with coefficients ϵ^0 and ϵ^1, respectively, are collected. Equating them each to zero, the following equations are obtained:

$$\mathcal{O}(\epsilon^0): \frac{\partial^2 r_0}{\partial t^2} + 2\zeta\frac{\partial r_0}{\partial t} + \kappa r_0 + k_4 r_0(t-\tau) = 0 \tag{50a}$$

$$\mathcal{O}(\epsilon^1): \frac{\partial^2 r_1}{\partial t^2} + 2\zeta\frac{\partial r_1}{\partial t} + \kappa r_1 + k_4 r_1(t-\tau) - k_2\Delta r_0 + 2\zeta\frac{\partial r_0}{\partial T_0} - k_4\tau\frac{\partial r_0(t-\tau)}{\partial T_0} + 2\frac{\partial^2 r_0}{\partial T_0 \partial t} + k_3 r_0^3 = 0 \tag{50b}$$

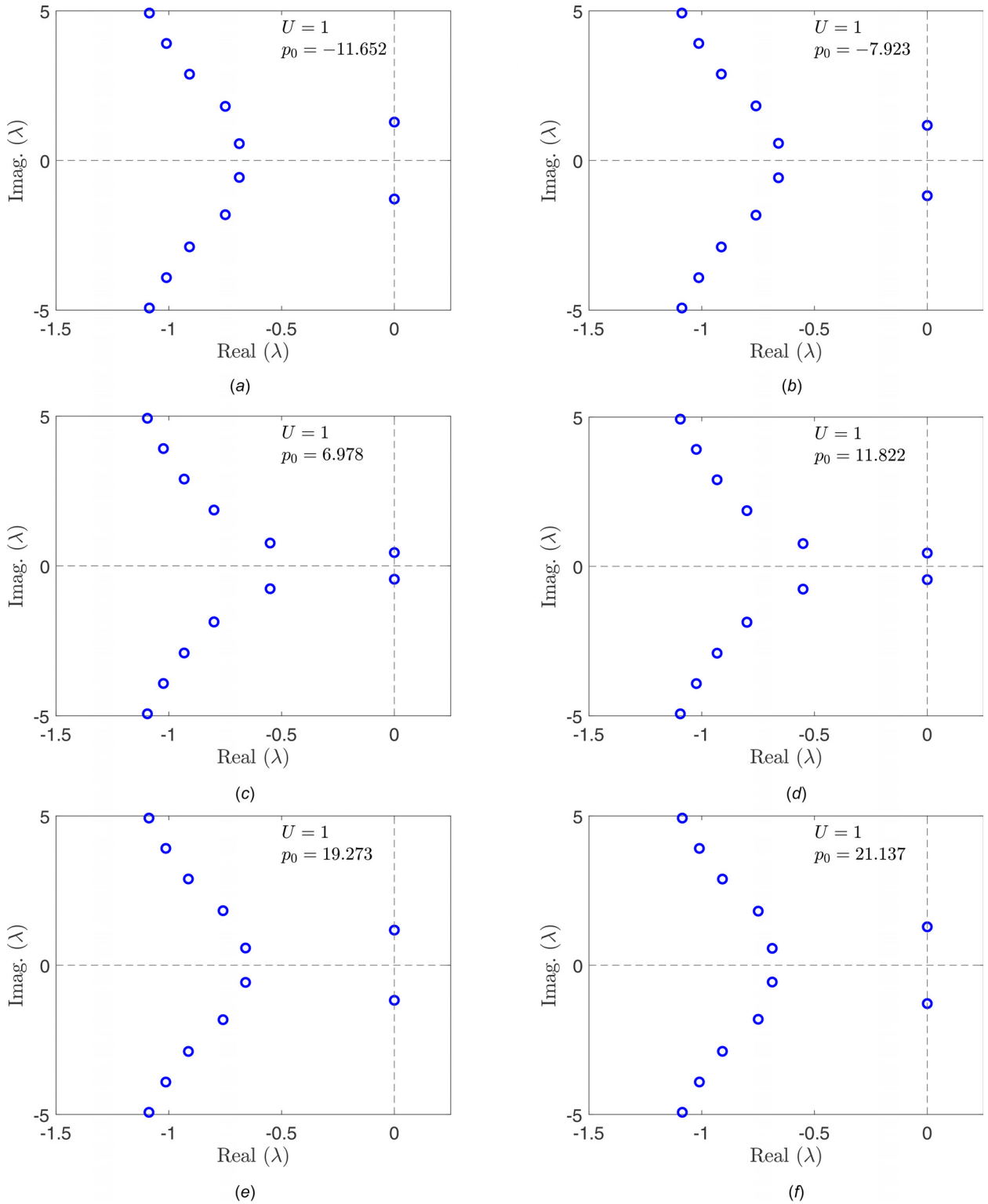

Fig. 6 Characteristic roots of Eq. (14), obtained using Galerkin approximations for $U = 1$ and for (*a*) $p_0 = -11.652$, (*b*) $p_0 = -7.923$, (*c*) $p_0 = 6.978$, (*d*) $p_0 = 11.822$, (*e*) $p_0 = 19.273$, and (*f*) $p_0 = 21.137$.

At the Hopf bifurcation point, the transient solution of Eq. (50*a*) decays with time since the characteristic roots lie on the left half of the complex plane (see Figs. 6(*a*)–6(*c*)). The only solution that persists is the one due to the roots lying on the imaginary axis, with frequency ω_{cr}. Therefore, the solution of Eq. (50*a*) is assumed as follows:

$$r_0(t,T_0) = A(T_0)\sin(\omega_{cr}t) + B(T_0)\cos(\omega_{cr}t) \tag{51}$$

Substituting Eq. (51) in Eq. (50*b*), we get

$$\frac{\partial^2 r_1}{\partial t^2} + 2\zeta\frac{\partial r_1}{\partial t} + \kappa r_1 + k_4 r_1(t-\tau) + Z_1\cos(3\omega_{cr}t) + Z_2\sin(3\omega_{cr}t) + Z_3\cos(\omega_{cr}t) + Z_4\sin(\omega_{cr}t) = 0 \tag{52}$$

where Z_1, Z_2, Z_3, and Z_4 are given as follows:

$$Z_1 = \frac{1}{4}k_3B^3 - \frac{3}{4}k_3A^2B \tag{53a}$$

$$Z_2 = \frac{1}{4}k_3A^3 + \frac{3}{4}k_3AB^2 \tag{53b}$$

$$Z_3 = \left(k_4\tau\sin(\omega_{cr}\tau) + 2\omega\right)\frac{\partial A}{\partial T_0} + \left(2\zeta - k_4\tau\cos(\omega_{cr}\tau)\right)\frac{\partial B}{\partial T_0} + \frac{3}{4}k_3A^2B + \frac{3}{4}k_3B^3 - k_2\Delta B \tag{53c}$$

$$Z_4 = \left(2\zeta - k_4\tau\cos(\omega_{cr}\tau)\right)\frac{\partial A}{\partial T_0} - \left(2\omega_{cr} + k_4\tau\sin(\omega\tau)\right)\frac{\partial B}{\partial T_0} + \frac{3}{4}k_3AB^2 + \frac{3}{4}k_3A^3 - k_2\Delta A \tag{53d}$$

The terms with coefficients Z_3 and Z_4 cause resonance in Eq. (52) and are known as secular terms. Since the solution of $r(t)$ is bounded, these terms should vanish. Setting $Z_3 = 0$ and $Z_4 = 0$, the expressions for $(\partial A/\partial T_0)$ and $(\partial B/\partial T_0)$ are obtained. Then, using the relations $\dot{A} = \epsilon(\partial A/\partial T_0) + \mathcal{O}(\epsilon^2)$ and $\dot{B} = \epsilon(\partial B/\partial T_0) + \mathcal{O}(\epsilon^2)$, the complex amplitude modulation relations are obtained as follows:

$$\dot{A}(t) = \epsilon\left(\frac{A_1\sin(\omega_{cr}\tau) + A_2\cos(\omega_{cr}\tau) + A_3}{4A_4}\right) \tag{54a}$$

$$\dot{B}(t) = \epsilon\left(\frac{B_1\sin(\omega_{cr}\tau) + B_2\cos(\omega_{cr}\tau) + B_3}{4B_4}\right) \tag{54b}$$

In Eq. (54*a*), the variables A_1–A_4 are given by

$$A_1 = 3k_4\tau k_3B^3 - 4Bk_4\tau k_2\Delta + 3Bk_4\tau k_3A^2 \tag{55a}$$

$$A_2 = -3k_3AB^2k_4\tau - 3k_3A^3k_4\tau + 4k_2\Delta Ak_4\tau \tag{55b}$$

$$A_3 = 6k_3AB^2\zeta + 6k_3A^3\zeta - 8k_2\Delta A\zeta + 6\omega_{cr}k_3B^3 - 8B\omega_{cr}k_2\Delta + 6B\omega_{cr}k_3A^2 \tag{55c}$$

$$A_4 = -k_4^2\tau^2 + 4k_4\tau\cos(\omega_{cr}\tau)\zeta - 4\zeta^2 - 4\omega_{cr}^2 - 4\omega k_4\tau\sin(\omega_{cr}\tau) \tag{55d}$$

In Eq. (54*b*), the variables B_1–B_4 are given as follows:

$$B_1 = -3k_3AB^2k_4\tau - 3k_3A^3k_4\tau + 4k_2\Delta Ak_4\tau \tag{56a}$$

$$B_2 = 4Bk_4\tau k_2\Delta - 3k_4\tau k_3B^3 - 3Bk_4\tau k_3A^2 \tag{56b}$$

$$B_3 = -6\omega_{cr}k_3A^3 + 6k_3B^3\zeta - 8Bk_2\Delta\zeta - 6\omega_{cr}k_3AB^2 + 8\omega_{cr}k_2\Delta A + 6Bk_3A^2\zeta \tag{56c}$$

$$B_4 = -k_4^2\tau^2 + 4k_4\tau\cos(\omega_{cr}\tau)\zeta - 4\zeta^2 - 4\omega_{cr}^2 - 4\omega_{cr}k_4\tau\sin(\omega_{cr}\tau) \tag{56d}$$

Now, using the polar transformation $A(t) = R(t)\sin(\theta(t))$ and $B(t) = R(t)\cos(\theta(t))$ in Eqs. (54*a*) and (54*b*), the amplitude and phase modulation equations are obtained as follows:

$$\dot{R}(t) = \epsilon e_1\left(4k_2\Delta R(t) - 3k_3R(t)^3\right) \tag{57a}$$

$$\dot{\theta}(t) = \epsilon e_2\left(4k_2\Delta - 3k_3R(t)^2\right) \tag{57b}$$

where e_1 and e_2 are defined as follows:

$$e_1 = \left(k_4\tau\cos(\omega_{cr}\tau) - 2\zeta\right)/e_3 \tag{58a}$$

$$e_2 = \left(2\omega_{cr} + k_4\tau\sin(\omega_{cr}\tau)\right)/e_3 \tag{58b}$$

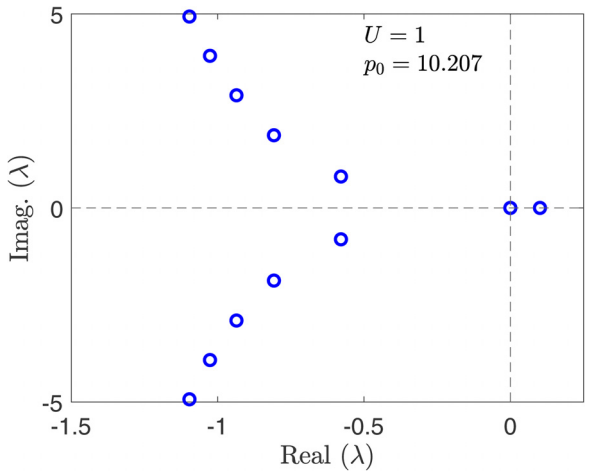

Fig. 7 Characteristic roots of Eq. (14) obtained using Galerkin approximations for $U = 1$ and for $p_0 = 10.207$

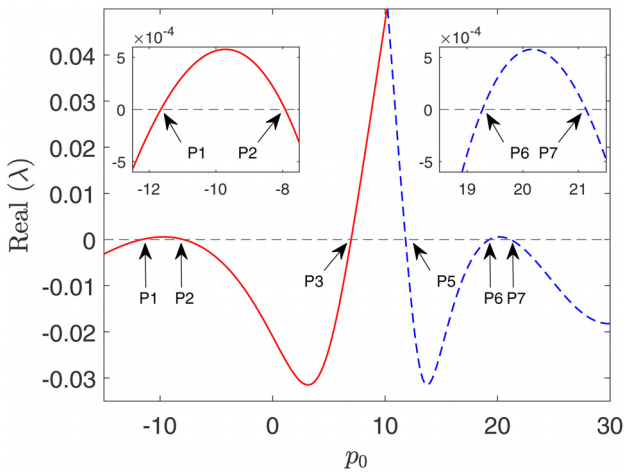

Fig. 8 Variation of the real part of rightmost characteristic root of Eq. (14) for $U = 1$ and for $-15 \le p_0 \le 30$

Here, $e_3 = 4(-k_4^2\tau^2 + 4k_4\tau\cos(\omega_{cr}\tau)\zeta - 4\zeta^2 - 4\omega_{cr}^2 - 4\omega_{cr}k_4\tau\sin(\omega_{cr}\tau))$. The approximate solution of the DDE presented in Eq. (47), accurate to $\mathcal{O}(\epsilon^0)$, can now be written using the normal-form equations (Eqs. (57*a*) and (57*b*)) as follows:

$$r(t) \approx R(t)\cos(\omega_{cr}t + \theta(t)) \tag{59a}$$

$$\dot{r}(t) \approx \dot{R}(t)\cos(\omega_{cr}t + \theta(t)) - R(t)\sin(\omega_{cr}t + \theta(t))\big(\omega_{cr} + \dot{\theta}(t)\big) \tag{59b}$$

4.1.1 Hopf Bifurcation at Point P_1. Substituting the values of p_{cr} and ω_{cr} for point P_1 (see Table 1) in Eqs. (57*a*) and (57*b*), we get

$$\dot{R}(t) = 5.7073 \times 10^{-4}(\epsilon\Delta)R(t) - 6.1730 \times 10^{-3}R(t)^3 \tag{60a}$$

$$\dot{\theta}(t) = 2.8203 \times 10^{-2}(\epsilon\Delta) - 30.5050 \times 10^{-2}R(t)^2 \tag{60b}$$

Figure 9(*a*) shows the local bifurcation diagram (supercritical Hopf bifurcation) obtained from Eq. (60*a*). In all the bifurcation diagrams reported in this paper, solid lines are used to represent stable solutions, while dashed lines are used to represent the unstable solutions. Also, nonzero equilibrium solutions ($R \neq 0$) correspond to the amplitudes of the periodic solutions that arise from the Hopf bifurcation. The blue circles in Fig. 9(*a*) are the amplitudes of the periodic solutions obtained by integrating Eq. (47) using the *dde*23 MATLAB solver. Equation (47) is a DDE for which the history function must be defined for numerical integration. First, with initial conditions $R(0)$ and $\theta(0)$, the set of ODEs given by Eqs. (60*a*) and (60*b*) are solved. Then, $r(t)$ (Eq. (59*a*)) and $\dot{r}(t)$ (Eq. (59*b*)) obtained for the interval $[0, \tau]$ ($\tau = (2\pi/U)$) is given as the history function for Eq. (47). Figures 9(*b*) (for $\epsilon\Delta = -0.1$) and 9(*c*) (for $\epsilon\Delta = 0.1$) show $R(t)$ obtained using Eq. (60*a*) (red line) and the system response $r(t)$, obtained by integrating Eq. (47) using the *dde*23 MATLAB solver (blue line).

Figures 9(*a*) and 9(*b*) indicate that for $\epsilon\Delta < 0$, the system settles at the zero equilibrium (solid black line in Fig. 9(*a*)) for any initial condition. For $\epsilon\Delta > 0$ (see Figs. 9(*a*) and 9(*c*)), the system settles into a periodic motion whose amplitude is given by R^* corresponding to the value of $\epsilon\Delta$.

4.1.2 Hopf Bifurcation at Point P_2. Substituting the values of p_{cr} and ω_{cr} for point P_2 (see Table 1) in Eqs. (57*a*) and (57*b*), we get

$$\dot{R}(t) = -6.7009 \times 10^{-4}(\epsilon\Delta)R(t) + 7.2477 \times 10^{-3}R(t)^3 \tag{61a}$$

$$\dot{\theta}(t) = 3.0835 \times 10^{-2}(\epsilon\Delta) - 33.3519 \times 10^{-2}R(t)^2 \tag{61b}$$

Figure 10(*a*) shows the local bifurcation diagram (subcritical Hopf bifurcation) obtained from Eq. (61*a*). For a given $\epsilon\Delta$, the amplitude of unstable periodic solutions is obtained from Eq. (47) as follows. We numerically integrate Eq. (47) for increasing values of constant history function and track the equilibrium solution. The critical value of the magnitude of the history function, above which the equilibrium will not approach zero, is considered to be the magnitude of the unstable limit cycle (blue circle). Figure 10(*b*) shows $R(t)$ obtained using Eq. (61*a*) (red line) and the system response $r(t)$ obtained by integrating Eq. (47) using the *dde*23 MATLAB solver (blue line). Both cases are for $\epsilon\Delta = 0.1$ and for the magnitude of history function given by point A1 in Fig. 10(*a*). Figure 10(*c*) shows the same physical quantities for the magnitude of the history function given by point A2 in Fig. 10(*a*).

Figures 10(*a*) and 10(*b*) indicate that for a given value of $\epsilon\Delta(>0)$, any initial condition greater than R^* results in a diverging solution. Conversely, for a given value of $\epsilon\Delta(>0)$, any initial condition less than R^* (see Figs. 10(*a*) and 10(*c*)) results in the system settling at the zero equilibrium (solid black line in Fig. 10(*a*)).

4.1.3 Hopf Bifurcation at Point P_3. Substituting the values of p_{cr} and ω_{cr} for point P_3 (see Table 1) in Eqs. (57*a*) and (57*b*), we get

$$\dot{R}(t) = 144.5864 \times 10^{-4}(\epsilon\Delta)R(t) - 156.3844 \times 10^{-3}R(t)^3 \tag{62a}$$

$$\dot{\theta}(t) = 7.8807 \times 10^{-2}(\epsilon\Delta) - 85.2384 \times 10^{-2}R(t)^2 \tag{62b}$$

Figure 11(*a*) shows the local bifurcation diagram (supercritical Hopf bifurcation) obtained from Eq. (62*a*). Figures 11(*a*)–11(*c*) are similar to Figs. 9(*a*)–9(*c*), except that these results are for the bifurcation point P_3. Figures 11(*a*) and 11(*b*) indicate that for $\epsilon\Delta < 0$, the system settles at the zero equilibrium (solid black line in Fig. 11(*a*)) for any initial condition. For $\epsilon\Delta > 0$ (see Figs. 11(*a*) and 11(*c*)), the system settles into a periodic motion whose amplitude is given by R^* corresponding to the value of $\epsilon\Delta$.

It can be seen from Figs. 9–11 that both the transient and the steady-state solutions of the normal-form equation, obtained using the MMS, match closely with the results from direct numerical integration.

4.2 Hopf Bifurcation for the Case of $\bar{q}=\bar{q}_2$. To study the Hopf bifurcation at buckled equilibrium ($\bar{q} = \bar{q}_2$), we substitute the value of $\bar{q}_2$ from Eq. (10) into Eq. (38). It should be noted that the "$\pm$" sign in front of the expression for $\bar{q}_2$ in Eq. (10) corresponds to the upward/downward buckled configuration of the beam. Here, we study the bifurcation corresponding to the upward configuration (+ve sign). Due to the symmetric nature of the buckling problem, the results are equally valid for the downward configuration (−ve sign). The characteristic equation corresponding to the linearized version of Eq. (38) around the equilibrium $\bar{q} = \bar{q}_2$ is given by

$$D(\lambda, p_0) = \lambda^2 + 2\zeta\lambda - 2k_1 + 2k_2p_0 - 3k_4 + k_4e^{-\lambda\tau} = 0 \tag{63}$$

The characteristic equation $D(\lambda, p_0)$ satisfies Eq. (43); therefore, we have

$$\frac{d\lambda}{dp_0} = \frac{-2k_2}{2\lambda + 2\zeta - k_4\tau e^{-\lambda\tau}} \tag{64}$$

At the Hopf bifurcation point, we have $p_0 = p_{cr}$ and $\lambda = j\omega_{cr}$. Substituting these values in Eq. (64), we get

$$\left.\frac{d\lambda}{dp_0}\right|_{p_0=p_{cr},\,\lambda=j\omega_{cr}} = \frac{-2k_2}{2j\omega_{cr} + 2\zeta - k_4\tau e^{-j\omega_{cr}\tau}} \tag{65}$$

With $\Gamma = \text{Real}(d\lambda/dp_0)|_{p_0=p_{cr},\,\lambda=j\omega_{cr}}$, we have

$$\Gamma = \frac{-2k_2\big(-2\zeta + k_4\tau\cos(\omega_{cr}\tau)\big)}{-4\zeta^2 + 4\zeta k_4\tau\cos(\omega_{cr}\tau) - k_4^2\tau^2 - 4\omega_{cr}^2 - 4\omega k_4\tau\sin(\omega_{cr}\tau)} \tag{66}$$

Substituting $\sin(\omega_{cr}\tau)$ and $\cos(\omega_{cr}\tau)$ obtained from Eqs. (18*a*) and (18*b*) in Eq. (66), we get

$$\Gamma = \frac{-2k_2\big(-2\zeta + \tau\big(\omega^2 + 2k_1 - 2k_2p_0 + 3k_4\big)\big)}{-4\zeta + 4\zeta\tau\big(\omega_{cr}^2 + 2k_1 - 2k_2p_0 + 3k_4\big) - k_4^2\tau^2 - 4\omega_{cr}^2 - 8\omega_{cr}^2\tau\zeta} \tag{67}$$

The velocity of root-crossing (Γ), calculated from Eq. (67), at points P_5, P_6, and P_7 (Fig. 5) is shown in the fourth column of Table 1. It can be seen from Table 1 that the analytically predicted

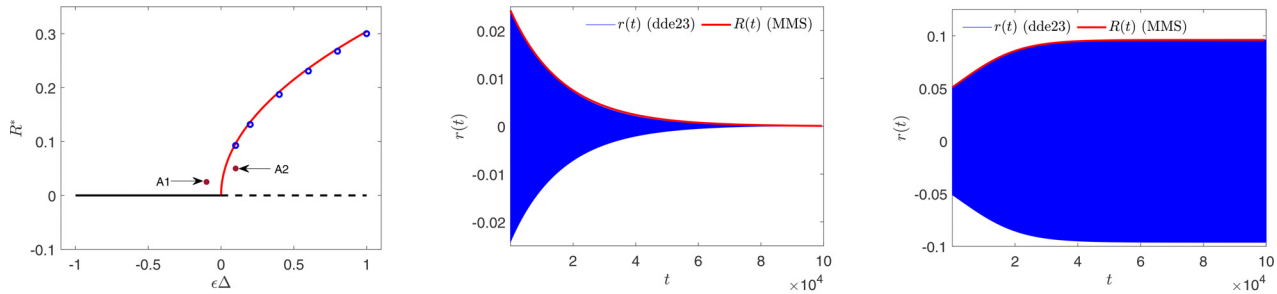

(*a*) (*b*) (*c*)

Fig. 9 (*a*) Local bifurcation diagram at point P_1. System response at local bifurcation point P_1 for (*b*) $\epsilon\Delta = -0.1$ with initial conditions for Eqs. (60*a*) and (60*b*) given by point A1 in (*a*) and (*c*) $\epsilon\Delta = 0.1$ with initial conditions for Eqs. (60*a*) and (60*b*) given by point A2 in (*a*).

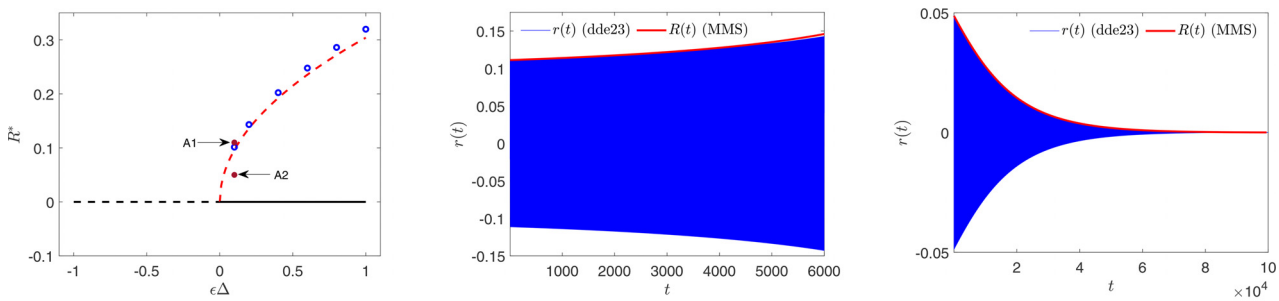

(*a*) (*b*) (*c*)

Fig. 10 (*a*) Local-bifurcation diagram at point P_2. System response at local bifurcation point P_2 for $\epsilon\Delta = 0.1$ with initial conditions for Eqs. (61*a*) and (61*b*) given in (*a*) by point (*b*) A1 and (*c*) A2.

values of Γ at the Hopf bifurcation points are in close agreement with those obtained numerically using Galerkin approximations. Furthermore, at the critical points (P_5, P_6, and P_7), we have $\Gamma \neq 0$ in both cases.

Next, the normal form equations for Eq. (38), around the Hopf bifurcation points for the equilibrium at $\bar{q} = \bar{q}_2$, are derived. As there is a quadratic nonlinearity in Eq. (38), we substitute $p_0 = p_{cr} + \epsilon^2\Delta$ and $\alpha_4 = \epsilon^2 k_3$ in Eq. (38) to obtain the normal form near the Hopf bifurcation point. Substituting the parameters ζ, k_1, k_2, k_4 (as defined in Eq. (40)), p_0 and α_4 in Eq. (38), we obtain

$$\ddot{r}(t) + 2\zeta\dot{r}(t) + \left[k_1 - \left(p_{cr} + \epsilon^2\Delta\right)k_2 + 3\epsilon^2 k_3 \bar{q}_2^2\right] r(t) + 3\epsilon^2 k_3 \bar{q}_2 r(t)^2 + \epsilon^2 k_3 r(t)^3 + k_4 r(t-\tau) = 0 \tag{68}$$

Substituting the parameters k_1, k_2, k_3, k_4, ϵ^2, and Δ in Eq. (10), we get

$$\bar{q}_2 = \sqrt{\frac{-\alpha_3\left[1 - \dfrac{p_0}{\pi^2}\right] - \alpha_5 U^2}{\alpha_4}} = \sqrt{\frac{-k_4 - k_1 + k_2 p_{cr} + k_2\epsilon^2\Delta}{\epsilon^2 k_3}} \tag{69}$$

Substituting Eq. (69) into Eq. (68), we get

$$\ddot{r}(t) + 2\zeta\dot{r}(t) + \left(2k_2 p_{cr} - 2k_1 - 3k_4 + 2k_2\epsilon^2\Delta\right) r(t) + \epsilon^2 k_3 r(t)^3 + 3\epsilon\sqrt{k_3(-k_4 - k_1 + k_2 p_{cr} + k_2\epsilon^2\Delta)}\, r(t)^2 + k_4 r(t-\tau) = 0 \tag{70}$$

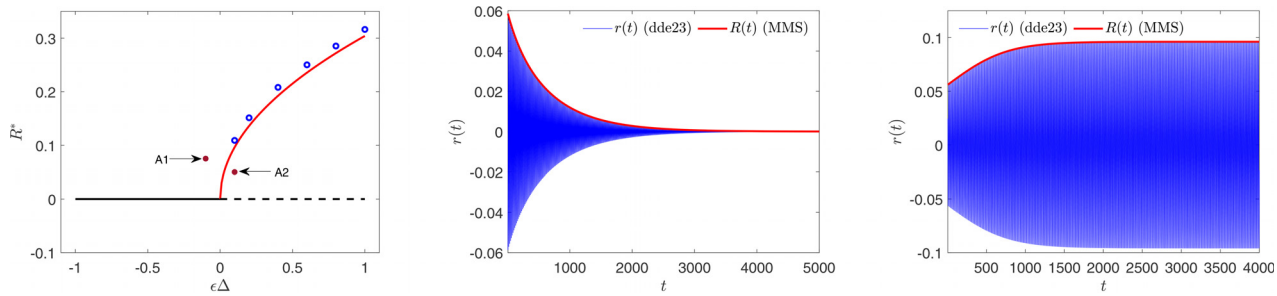

(*a*) (*b*) (*c*)

Fig. 11 (*a*) Local bifurcation diagram at point P_3. System response at local bifurcation point P_3 for (*b*) $\epsilon\Delta = -0.1$ with initial conditions for Eqs. (61*b*) and (62*b*) given by point A1 in (*a*) and (*c*) $\epsilon\Delta = 0.1$ with initial conditions for Eqs. (62*b*) and (62*b*) given by point A2 in (*a*).

Next, expanding the square-root term in Eq. (70) using the Taylor series around $\epsilon = 0$, we get

$$\sqrt{k_3(-k_4 - k_1 + k_2 p_{cr} + k_2 \epsilon^2 \Delta)} \approx a_1 - a_2 \epsilon^2 \Delta \tag{71}$$

where $a_1 = \sqrt{-k_3(k_4 + k_1 - k_2 p_{cr})}$ and $a_2 = (1/2)\left(\sqrt{-k_3(k_4 + k_1 - k_2 p_{cr})} k_2 / k_4 + k_1 - k_2 p_{cr}\right)$. Substituting Eq. (71) into Eq. (70), we get

$$\ddot{r}(t) + 2\zeta \dot{r}(t) + \left(a_3 + a_4 \epsilon^2 \Delta\right) r(t) + 3\epsilon\left(a_1 - a_2 \epsilon^2 \Delta\right) r(t)^2 + \epsilon^2 k_3 r(t)^3 + k_4 r(t-\tau) = 0 \tag{72}$$

where $a_3 = 2k_2 p_{cr} - 2k_1 - 3k_4$ and $a_4 = 2k_2$. Now, introducing the new time scales $T_0 = \epsilon^1 t$ and $T_1 = \epsilon^2 t$, $r(t)$ is expanded as follows:

$$r(t) = r(t, T_0, T_1) = r_0(t, T_0, T_1) + \epsilon r_1(t, T_0, T_1) + \epsilon^2 r_2(t, T_0, T_1) + \cdots \tag{73}$$

In Eq. (73), $t = \epsilon^0 t$ is the actual time-scale; T_0 and T_1 are the slow time-scales. The time-delay term $r(t-\tau)$ is expanded up to $\mathcal{O}(\epsilon^2)$ using the Taylor series similar to Eq. (49). Upon substituting the expressions for $r(t-\tau)$ and $r(t)$ in Eq. (72), terms with coefficients of ϵ^0, ϵ^1, and ϵ^2 are collected and are each equated to zero to obtain the following equations:

$$\mathcal{O}(\epsilon^0): \frac{\partial^2 r_0}{\partial t^2} + 2\zeta \frac{\partial r_0}{\partial t} + a_3 r_0 + k_4 r_0(t-\tau) = 0 \tag{74a}$$

$$\mathcal{O}(\epsilon^1): \frac{\partial^2 r_1}{\partial t^2} + 2\zeta \frac{\partial r_1}{\partial t} + a_3 r_1 + k_4 r_1(t-\tau) = \tau k_4 \frac{\partial r_0(t-\tau)}{\partial T_0} - 2\frac{\partial^2 r_0}{\partial T_0 \partial t} - 2\zeta \frac{\partial r_0}{\partial T_0} - 3a_1 r_0^2 \tag{74b}$$

$$\mathcal{O}(\epsilon^2): \frac{\partial^2 r_2}{\partial t^2} + 2\zeta \frac{\partial r_2}{\partial t} + a_3 r_2 + k_4 r_2(t-\tau) = K_1 + K_2 + K_3 - 6 r_0 r_1 a_1 \tag{74c}$$

where K_1, K_2, and K_3 are given as follows:

$$K_1 = -\left(a_4 \Delta r_0 + k_3 r_0^3 + 2\frac{\partial^2 r_0}{\partial T_1 \partial t} + \frac{\partial^2 r_0}{\partial T_0^2}\right) \tag{75a}$$

$$K_2 = -\left(2\zeta \frac{\partial r_0}{\partial T_1} - k_4 \tau \frac{\partial r_0(t-\tau)}{\partial T_1} + \frac{1}{2}\tau^2 k_4 \frac{\partial^2 r_0(t-\tau)}{\partial T_0^2}\right) \tag{75b}$$

$$K_3 = -\left(2\frac{\partial^2 r_1}{\partial T_0 \partial t} + 2\zeta \frac{\partial r_1}{\partial T_0} - k_4 \tau \frac{\partial r_1(t-\tau)}{\partial T_0}\right) \tag{75c}$$

Since the only nondecaying solution at the Hopf bifurcation point is the one due to the roots lying on the imaginary axis with frequency ω_{cr}, the solution of Eq. (74a) can be written as follows:

$$r_0(t, T_0, T_1) = A(T_0, T_1)\cos(\omega_{cr} t) + B(T_0, T_1)\sin(\omega_{cr} t) \tag{76}$$

Substituting Eq. (76) into Eq. (74b), we get

$$\frac{\partial^2 r_1}{\partial t^2} + 2\zeta \frac{\partial r_1}{\partial t} + a_3 r_1 + k_4 r_1(t-\tau) = -Z_5 \cos(\omega_{cr} t) - Z_6 \sin(\omega_{cr} t) - Z_7 \cos(2\omega_{cr} t) - Z_8 \sin(2\omega_{cr} t) - Z_9 \tag{77}$$

where Z_5, Z_6, Z_7, Z_8, and Z_9 are given by

$$Z_5 = -k_4 \tau \frac{\partial A}{\partial T_0}\cos(\omega_{cr}\tau) + k_4 \tau \frac{\partial B}{\partial T_0}\sin(\omega_{cr}\tau) + 2\zeta \frac{\partial A}{\partial T_0} + 2\frac{\partial B}{\partial T_0}\omega_{cr} \tag{78a}$$

$$Z_6 = 2\zeta \frac{\partial B}{\partial T_0} - 2\frac{\partial A}{\partial T_0}\omega_{cr} - k_4 \tau \frac{\partial A}{\partial T_0}\sin(\omega_{cr}\tau) - k_4 \tau \frac{\partial B}{\partial T_0}\cos(\omega_{cr}\tau) \tag{78b}$$

$$Z_7 = \frac{3}{2}a_1 A^2 - \frac{3}{2}a_1 B^2 \tag{78c}$$

$$Z_8 = 3a_1 AB \tag{78d}$$

$$Z_9 = \frac{3}{2}a_1 A^2 + \frac{3}{2}a_1 B^2 \tag{78e}$$

In order to eliminate the secular terms, we set $Z_5 = 0$ and $Z_6 = 0$. Equations (78a) and (78b) then give us

$$\frac{\partial A}{\partial T_0} = 0 \tag{79a}$$

$$\frac{\partial B}{\partial T_0} = 0 \tag{79b}$$

Equation (77) is now rewritten as

$$\frac{\partial^2 r_1}{\partial t^2} + 2\zeta \frac{\partial r_1}{\partial t} + a_3 r_1 + k_4 r_1(t-\tau) + Z_7 \cos(2\omega_{cr} t) + Z_8 \sin(2\omega_{cr} t) + Z_9 = 0 \tag{80}$$

The solution $r_1(t, T_0, T_1)$ of Eq. (80) is assumed as follows:

$$r_1(t, T_0, T_1) = C_1(T_0, T_1) + C_2(T_0, T_1)\cos(2\omega_{cr} t) + C_3(T_0, T_1)\sin(2\omega_{cr} t) \tag{81}$$

Substituting Eq. (81) in Eq. (80) and solving for C_1, C_2, and C_3, we get

$$C_1 = -\frac{3}{2}\frac{a_1(A^2 + B^2)}{k_4 + a_3} \tag{82a}$$

$$C_2 = \frac{h_1 \cos(2\omega_{cr}\tau) + h_2 \sin(2\omega_{cr}\tau) + h_3}{h_4} \tag{82b}$$

$$C_3 = \frac{h_5 \cos(2\omega_{cr}\tau) + h_6 \sin(2\omega_{cr}\tau) + h_7}{h_8} \tag{82c}$$

where h_1–h_8 are defined as follows:

$$h_1 = -3a_1 k_4 B^2 + 3a_1 k_4 A^2 \tag{83a}$$

$$h_2 = 6a_1 AB k_4 \tag{83b}$$

$$h_3 = -24a_1 AB\omega_{cr}\zeta - 12a_1\omega_{cr}^2 A^2 + 12a_1\omega_{cr}^2 B^2 - 3a_1 a_3 B^2 + 3a_1 a_3 A^2 \tag{83c}$$

$$h_4 = \left(-4k_4a_3 + 16\omega_{cr}^2k_4\right)\cos(2\omega_{cr}\tau) - 2k_4^2 + 16k_4\zeta\omega_{cr}\sin(2\omega_{cr}\tau) - 32\zeta^2\omega_{cr}^2 - 2a_3^2 - 32\omega_{cr}^4 + 16\omega_{cr}^2a_3 \tag{83d}$$

$$h_5 = 3a_1B^2k_4 - 3a_1A^2k_4 \tag{83e}$$

$$h_6 = 6a_1ABk_4 \tag{83f}$$

$$h_7 = -24a_1AB\omega_{cr}^2 + 12a_1A^2\zeta\omega_{cr} - 12a_1B^2\zeta\omega_{cr} + 6a_1a_3AB \tag{83g}$$

$$h_8 = \left(-4k_4a_3 + 16\omega_{cr}^2k_4\right)\cos(2\omega_{cr}\tau) - 2k_4^2 + 16k_4\zeta\omega_{cr}\sin(2\omega_{cr}\tau) - 32\zeta^2\omega_{cr}^2 - 2a_3^2 - 32\omega_{cr}^4 + 16\omega_{cr}^2a_3 \tag{83h}$$

Substituting Eqs. (73) and (81) in Eq. (74*c*) and by setting the coefficients of secular terms to zero, we solve for $(\partial A/\partial T_1)$ and $(\partial B/\partial T_1)$. Then, using the relations $\dot{A} = \epsilon(\partial A/\partial T_0) + \epsilon^2(\partial A/\partial T_1)$ and $\dot{B} = \epsilon(\partial B/\partial T_0) + \epsilon^2(\partial B/\partial T_1)$, and substituting $(\partial A/\partial T_0) = (\partial B/\partial T_0) = 0$ (see Eqs. (79*a*) and (79*b*)) in $\dot{A}$ and $\dot{B}$, we note that

$$\dot{A} = \epsilon^2\frac{\partial A}{\partial T_1} \tag{84a}$$

$$\dot{B} = \epsilon^2\frac{\partial B}{\partial T_1} \tag{84b}$$

Now, substituting the polar transformation $A(t) = R(t)\sin(\theta(t))$ and $B(t) = R(t)\cos(\theta(t))$ in Eqs. (84*a*) and (84*b*) and simplifying, the amplitude and phase modulation equations can be written as follows:

$$\dot{R}(t) = R_1\epsilon^2\Delta R(t) + R_2R^3(t) \tag{85a}$$

$$\dot{\theta}(t) = \theta_1\epsilon^2\Delta + \theta_2R^2(t) \tag{85b}$$

The approximate solution of the DDE presented in Eq. (72), accurate to $\mathcal{O}(\epsilon^0)$, can now be written using the normal form equations (Eqs. (85*a*) and (85*b*)) as follows:

$$r(t) \approx R(t)\cos(\omega_{cr}t + \theta(t)) \tag{86a}$$

$$\dot{r}(t) \approx \dot{R}(t)\cos(\omega_{cr}t + \theta(t)) - R(t)\sin(\omega_{cr}t + \theta(t))\left(\omega_{cr} + \dot{\theta}(t)\right) \tag{86b}$$

4.2.1 Hopf Bifurcation at Point P_5. Substituting the values of p_{cr} and ω_{cr} for point P_5 (see Table 1) in Eqs. (85*a*) and (85*b*), we get

$$\dot{R}(t) = -289.1699178\times10^{-4}(\epsilon^2\Delta)R(t) + 498.7098850\times10^{-3}R(t)^3 \tag{87a}$$

$$\dot{\theta}(t) = 15.76079909\times10^{-2}(\epsilon^2\Delta) - 3.121840462R(t)^2 \tag{87b}$$

Figure 12(*a*) shows the local bifurcation diagram (subcritical Hopf bifurcation) obtained from Eq. (87*a*). To obtain the amplitude of unstable periodic solutions, we numerically integrate Eq. (72) for a given $\epsilon^2\Delta$ and for increasing values of the constant history function, and track the equilibrium solution. The critical value of the magnitude of the history function above which the equilibrium will not approach zero is considered the magnitude of the unstable limit cycle (blue circle). Figure 12(*b*) shows $R(t)$ obtained using Eq. (87*a*) (red line) and the system response (blue line) obtained by integrating Eq. (72) using the *dde*23 MATLAB solver. Both cases are for $\epsilon^2\Delta = 0.01$ and the magnitude of the history function given by point A1 in Fig. 12(*a*). Figure 12(*c*) shows the same physical quantities for the magnitude of the history function given by point A2 in Fig. 12(*a*).

Figures 12(*a*) and 12(*b*) indicate that for a given value of $\epsilon^2\Delta(>0)$, any initial condition greater than R^* results in a diverging solution. On the contrary, for a given value of $\epsilon^2\Delta(>0)$, any initial condition less than R^* (see Figs. 12(*a*) and 12(*c*)) results in the system settling at the buckled equilibrium (solid black line in Fig. 12(*a*)).

4.2.2 Hopf Bifurcation at Point P_6. Substituting the values of p_{cr} and ω_{cr} for point P_6 (see Table 1) in Eqs. (85*a*) and (85*b*), we get

$$\dot{R}(t) = 13.18331333\times10^{-4}(\epsilon^2\Delta)R(t) - 30.54194023\times10^{-3}R(t)^3 \tag{88a}$$

$$\dot{\theta}(t) = 6.161982410\times10^{-2}(\epsilon^2\Delta) - 1.331671312R(t)^2 \tag{88b}$$

Figure 13(*a*) shows the local bifurcation diagram (supercritical Hopf bifurcation) obtained from Eq. (88*a*). Figures 13(*b*) (for $\epsilon^2\Delta = -0.01$) and 13(*c*) (for $\epsilon^2\Delta = 0.01$) show $R(t)$ obtained using Eq. (88*a*) (red line) and the system response obtained by integrating Eq. (72) using the *dde*23 MATLAB solver (blue line). Figures 13(*a*) and 13(*b*) indicate that for $\epsilon^2\Delta < 0$, the system settles at the buckled equilibrium (solid black line in Fig. 13(*a*)) for any initial condition. For $\epsilon^2\Delta > 0$ (see Figs. 13(*a*) and 13(*c*)), the system settles into a periodic motion whose amplitude is given by R^* corresponding to the value of $\epsilon^2\Delta$.

4.2.3 Hopf Bifurcation at Point P_7. Substituting the values of p_{cr} and ω_{cr} for point P_7 (see Table 1) in Eqs. (85*a*) and (85*b*), we get

$$\dot{R}(t) = -11.35943198\times10^{-4}(\epsilon^2\Delta)R(t) + 20.63464775\times10^{-3}R(t)^3 \tag{89a}$$

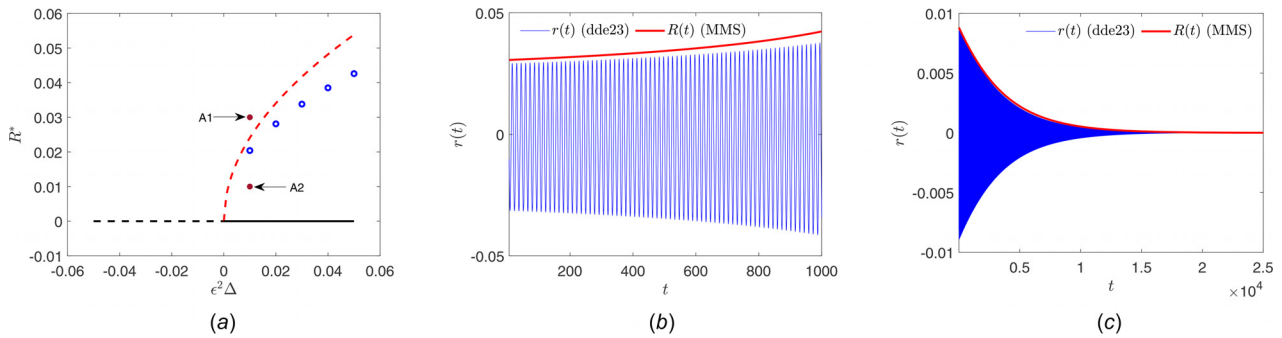

Fig. 12 (*a*) Local bifurcation diagram at point P_5. System response at local bifurcation point P_5 for $\epsilon^2\Delta = 0.01$ with initial conditions for Eqs. (87*a*) and (87*b*) given in (*a*) by point (*b*) A1 and (*c*) A2.

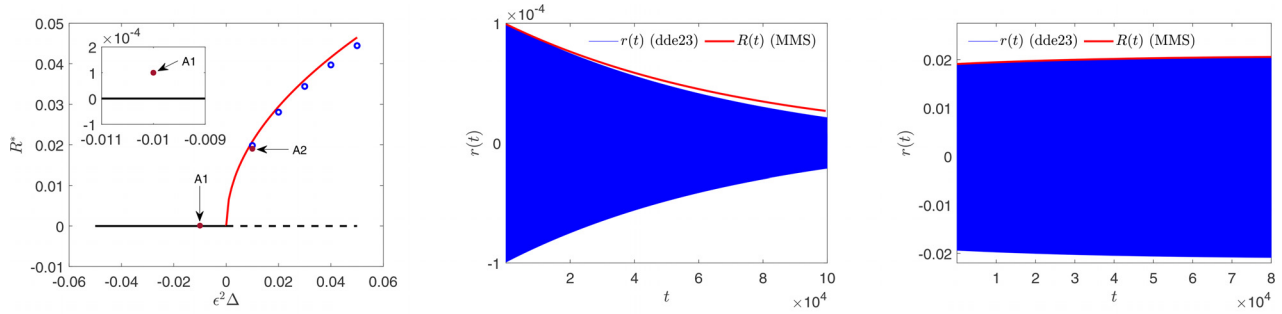

Fig. 13 (*a*) Local bifurcation diagram at point P_6. System response at local bifurcation point P_6 for (*b*) $\epsilon^2\Delta = -0.01$ with initial conditions for Eqs. (88*a*) and (88*b*) given by point A1 in (*a*) and for (*c*) $\epsilon^2\Delta = 0.01$ with initial conditions for Eqs. (88*a*) and (88*b*) given by point A2 in (*a*).

$$\dot{\theta}(t) = 5.641822544 \times 10^{-2}(\epsilon^2\Delta) - 1.215852977R(t)^2 \quad (89b)$$

Figure 14(*a*) shows the local bifurcation diagram (subcritical Hopf bifurcation) obtained from Eq. (89*a*). Figures 14(*a*)–14(*c*) are similar to Figs. 12(*a*)–12(*c*), except that these results are for the bifurcation point P_7. Figures 14(*a*) and 14(*b*) indicate that for a given value of $\epsilon^2\Delta(>0)$, any initial condition greater than R^* results in a diverging solution. On the contrary, for a given value of $\epsilon^2\Delta(>0)$, any initial condition less than R^* (see Figs. 14(*a*) and 14(*c*)) results in the system settling at the buckled equilibrium (solid black line in Fig. 14(*a*)).

It can be seen from Figs. 12–14 that the transient and the steady-state solutions of the normal-form equations for buckled equilibrium, obtained using the MMS, both match closely with the results obtained from direct numerical integration. This implies that both the methods are appropriate choices for this study. The mutual consistency of the results also serves to authenticate the results themselves. It should also be noted that for this study, the results obtained using the MMS were computationally less expensive than the results obtained from direct numerical integration. This makes MMS a candidate approach for studying the Hopf bifurcations of such systems.

All the results obtained using the MMS reported in this section are valid for small values of ϵ. To study the behavior of the system far from the bifurcation points, we resort to numerics and generate a global bifurcation diagram. These results are described in Sec. 5.

5 Global Bifurcation Analysis

Figure 15 shows the global bifurcation diagram obtained by integrating Eq. (8) using the *dde*23 MATLAB solver, for $U = 1$ and varying the axial load p_0, with $p_0 \in [-15, 30]$. It can clearly be seen from Fig. 15 that P_1, P_2, P_3, P_5, P_6, and P_7 are the Hopf bifurcation points. Furthermore, it should be observed that from point P_4, a second equilibrium ($\bar{q} = \bar{q}_2$) coexists with the equilibrium given by $\bar{q} = \bar{q}_1$. Solid blue lines indicate the stable equilibrium points and dotted blue line indicate the unstable equilibrium points for $\bar{q} = \bar{q}_1 = 0$. Solid magenta lines are the stable equilibrium points and dotted magenta lines are the unstable equilibrium points for $\bar{q} = \bar{q}_2 = \pm\sqrt{(-\alpha_3[1-(p_0/\pi^2)] - \alpha_5 U^2/\alpha_4)}$. In Fig. 15, solid and dashed lines represent the stable and unstable solutions, respectively. The stable and unstable periodic solutions are tracked using the same method as described in Sec. 4.

It can be seen from Fig. 15 that the stable and unstable periodic solutions arising from P_1 and P_2 meet at the saddle-node bifurcation point SN_1. At SN_1, $p_0 = 20.41$, after which both stable and unstable periodic solutions arising from P_1 and P_2 cease to exist. SN_2 is the saddle-node bifurcation point for the stable and unstable periodic solutions arising from P_3 and P_5, respectively. SN_3 is the saddle-node bifurcation point for the stable and unstable periodic solutions arising from P_6 and P_7, respectively. The axial loads at SN_2 and SN_3 are 25.8 and 24.15, respectively. The following important observations can be made from Fig. 15.

(1) For $p_0 \in (P_1, SN_2]$, there exist multiple limit cycles (both stable and unstable) for the system, due to Hopf bifurcation at different points.
(2) The zero equilibrium is unstable in the intervals $[P_1, P_2]$, and P_3 and beyond. The buckled equilibrium is unstable over intervals $[P_4, P_5]$ and $[P_6, P_7]$. Since no stable static equilibrium exists in these regions, the system can only settle in a stable limit-cycle.

Figures 16(*a*)–16(*c*) show the limit-cycles for $p_0 = 1$, $p_0 = 13$, and $p_0 = 20$, respectively. For $p_0 = 1$ (Fig. 16(*a*)), two coexisting limit cycles are present: one originating from supercritical Hopf bifurcation at P_1 (stable limit cycle, red solid line) and the other from the subcritical Hopf bifurcation at P_2 (unstable limit cycle,

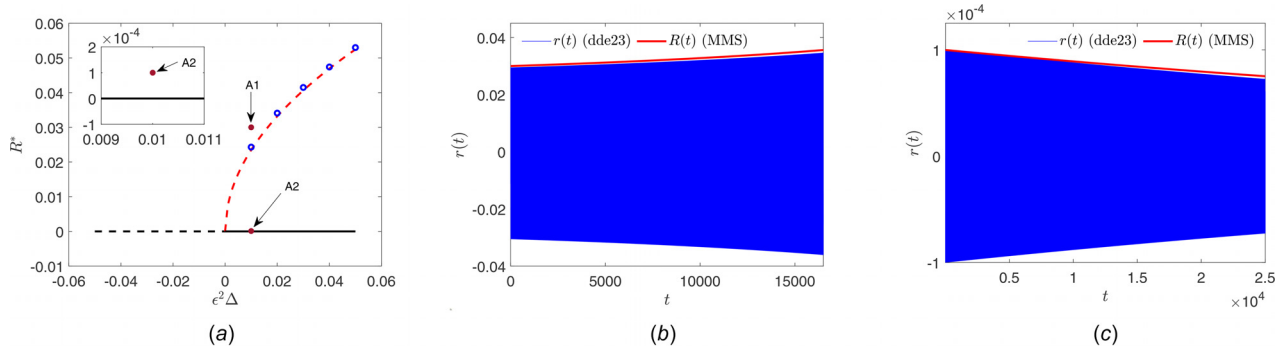

Fig. 14 (*a*) Local bifurcation diagram at point P_7. System response at local bifurcation point P_7 for $\epsilon^2\Delta = 0.01$ with initial conditions for Eqs. (88*a*) and (88*b*) given in Fig. 14(*a*) by point (*b*) A1 and (*c*) A2.

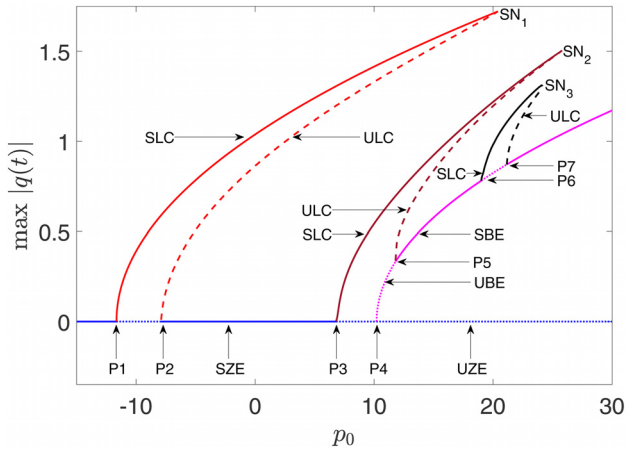

Fig. 15 Global bifurcation diagram of Eq. (8) for $U = 1$ and $p_0 \in [-15, 30]$. Stable limit-cycles arising from points P_1, P_3, and P_6 are denoted by SLC and the unstable limit-cycles arising from points P_2, P_5, and P_7 are denoted by ULC. Stable zero equilibrium is represented by blue solid line (SZE) and the unstable zero equilibrium is represented by dotted blue line (UZE). Magenta solid line represents the stable buckled equilibrium (SBE) and magenta dotted line represents the unstable buckled equilibrium (UBE).

red dashed line). For $p_0 = 13$ (Fig. 16(*b*)), four limit cycles coexist. Of these, two stable limit cycles arise from the supercritical Hopf bifurcation originating at points P_1 (red solid line) and P_3 (brown solid line), and two unstable limit cycles arise from the subcritical Hopf bifurcation originating at points P_2 (red dashed line) and P_5 (brown dashed line). For $p_0 = 20$ (Fig. 16(*c*)), five limit cycles coexist. Of these, three stable limit cycles arise from the supercritical Hopf bifurcation originating at points P_1 (red solid line), P_3 (brown solid line), and P_6 (black solid line), and two unstable limit cycles arise from the subcritical Hopf bifurcation originating at points P_2 (red dashed line) and P_5 (brown dashed line). Figure 16 should be contrasted with Fig. 15. All stable limit cycles for $p_0 = 1$, $p_0 = 13$, and $p_0 = 20$ are obtained by directly integrating the DDE given by Eq. (8). Obtaining unstable limit cycles for a system is a challenging task and hence the bisection method is used [47].

It can be seen that for $U = 1$, at lower axial loads (see Fig. 16(*a*)), the amplitude of stable limit-cycle oscillations is relatively less than that for higher axial loads (see Figs. 16(*b*) and 16(*c*)) making $p_0 \leq P_1$ a more favorable region to operate as the beam settles to zero equilibrium. The existence of multiple limit cycles at higher axial loads poses operational challenges because there are more than one settling amplitude, that depend on the initial conditions. Multiple limit cycles at higher values of axial load make fatigue life calculations more complicated in that region of the parametric space. However, if the operational conditions push the system into multiple limit-cycles region, fatigue-life calculations should be based on the worst case scenario of the limit-cycle amplitudes. It should be noted from the global bifurcation diagram that by inducing tensile loads, we can change p_0 from positive to negative and can control the region of operation of the heat exchanger. For example, if we apply sufficient tension and make $p_0 = -5$, the tube will be stable around zero equilibrium for flow velocity of $U = 1$.

6 Conclusions

The nonlinear dynamics of a heat-exchanger tube subjected to cross-flow has been studied. The critical curves for the resulting DDE are first obtained using an analytical approach. A Galerkin method is then used to analyze the stability of the system in the parametric space of flow velocity and axial (thermal) load. The analytical technique only gives the possible critical curves at which a stability switch may happen. However, using Galerkin approximations, the rightmost characteristic roots of the DDE in the $[U, p_0]$ plane are obtained to generate a more comprehensive stability chart. Furthermore, the damping present in the rightmost root, in the stable region, is obtained. The highest damping is present around $U = 2.34$ and $p_0 = 30$. The possibility of Hopf bifurcation has been investigated for $U = 1$. It is found that both zero and buckled equilibria can lose stability through supercritical or subcritical Hopf bifurcation. Using the MMS, normal forms near the bifurcation points have been obtained analytically. The results from local-bifurcation analysis using the MMS are in close agreement with numerical results indicating that both methods are appropriate for this study. The consistency of the results also serves to authenticate them. However, since the MMS is valid only in the immediate vicinity of the Hopf-bifurcation points, a global-bifurcation diagram has been generated using numerical simulations to analyze the tube motion farther away from the bifurcation points.

The presence of multiple co-existing limit-cycles at higher axial loads ($p_0 = 13$, and $p_0 = 20$) present operational challenges. This is due to the uncertainty in the settling amplitude that is contingent on the initial conditions of the vibrating tube, which in turn are hard to capture. Furthermore, the global-bifurcation diagram indicates that apart from Hopf bifurcations, three saddle-node bifurcation points also exist where the stable and unstable periodic solutions meet and cease to exist thereafter. The presence of saddle-node bifurcations implies that at certain values of axial load, the system can switch from one limit-cycle to another, which makes the behavior of the beam unpredictable.

The stability studies carried out in this work are expected to be useful in the designing of heat-exchanger tubes for greater tube life and safety. Therefore, for a given flow velocity, axial load can be tuned from the stability chart for maximum damping. Further, from the global bifurcation diagram, for a given flow velocity, axial load can be adjusted to suppress the limit cycle oscillations.

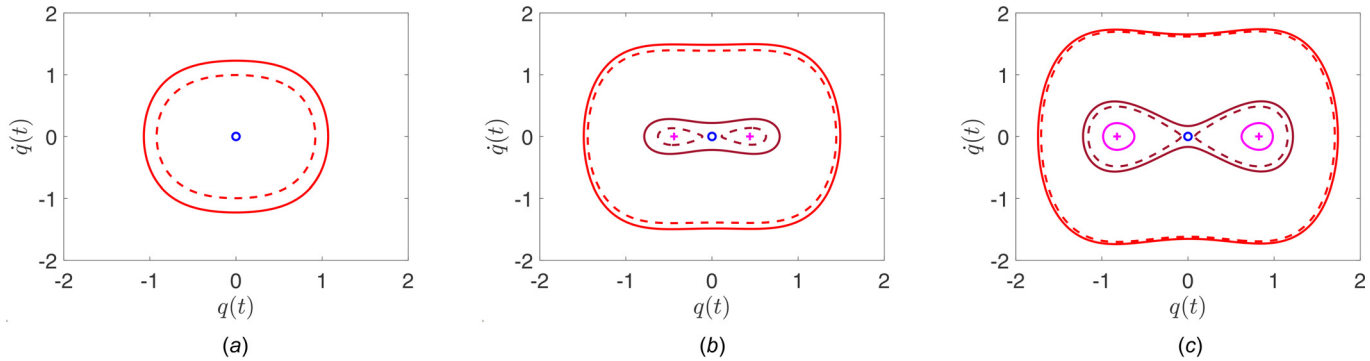

Fig. 16 (*a*) Limit-cycles for $U = 1$ with (*a*) $p_0 = 1$, (*b*) $p_0 = 13$, and (*c*) $p_0 = 20$

Acknowledgment

We thank anonymous reviewers for their insightful comments on an earlier version of this paper.

Funding Data

- Department of Science and Technology, Inspire fellowship (DST/INSPIRE/04/2014/000972; Funder ID: 10.13039/501100010218).

References

[1] Mitra, D. R., 2005, "Fluid-Elastic Instability in Tube Arrays Subjected to Air-Water and Steam-Water Cross-Flow," Ph.D. thesis, University of California, Los Angeles, CA.
[2] Chen, S., 1983, "Instability Mechanisms and Stability Criteria of a Group of Circular Cylinders Subjected to Cross-Flow—Part I: Theory," ASME J. Vib. Acoust., **105**(1), pp. 51–58.
[3] Price, S. J., and Paidoussis, M. P., 1986, "A Single-Flexible-Cylinder Analysis for the Fluidelastic Instability of an Array of Flexible Cylinders in Cross-Flow," ASME J. Fluids Eng., **108**(2), pp. 193–199.
[4] Khalifa, A., Weaver, D., and Ziada, S., 2012, "A Single Flexible Tube in a Rigid Array as a Model for Fluidelastic Instability in Tube Bundles," J. Fluids Struct., **34**, pp. 14–32.
[5] Roberto, B. W., 1962, "Low Frequency, Self-Excited Vibration in a Row of Circular Cylinders Mounted in an Airstream," Ph.D. thesis, University of Cambridge.
[6] Connors, H. J., 1970, "Fluidelastic Vibration of Tube Arrays Excited by Cross Flow," ASME Symposium on Flow-Induced Vibration in Heat Exchanger, Winter Annual Meeting, pp. 42–47.
[7] Blevins, R. D., 1974, "Fluid Elastic Whirling of a Tube Row," ASME J. Pressure Vessel Technol., **96**(4), pp. 263–267.
[8] Lever, J. H., and Weaver, D. S., 1986, "On the Stability of Heat Exchanger Tube Bundles—Part I: Modified Theoretical Model," J. Sound Vib., **107**(3), pp. 375–392.
[9] Paidoussis, M. P., and Li, G. X., 1992, "Cross-Flow-Induced Chaotic Vibrations of Heat-Exchanger Tubes Impacting on Loose Supports," J. Sound Vib., **152**(2), pp. 305–326.
[10] Tanaka, H., and Takahara, S., 1981, "Fluid Elastic Vibration of Tube Array in Cross Flow," J. Sound Vib., **77**(1), pp. 19–37.
[11] Dalton, C., and Helfinstine, R. A., 1971, "Potential Flow Past a Group of Circular Cylinders," ASME J. Fluids Eng., **93**(4), pp. 636–642.
[12] Païdoussis, M. P., Price, S. J., and De Langre, E., 2010, *Fluid-Structure Interactions: Cross-Flow-Induced Instabilities*, Cambridge University Press New York.
[13] Bazilevs, Y., Takizawa, K., and Tezduyar, T. E., 2013, *Computational Fluid-Structure Interaction: Methods and Applications*, Wiley, Hoboken, NJ.
[14] Wang, L., and Ni, Q., 2010, "Hopf Bifurcation and Chaotic Motions of a Tubular Cantilever Subject to Cross Flow and Loose Support," Nonlinear Dyn., **59**(1–2), pp. 329–338.
[15] Xia, W., and Wang, L., 2010, "The Effect of Axial Extension on the Fluidelastic Vibration of an Array of Cylinders in Cross-Flow," Nucl. Eng. Des., **240**(7), pp. 1707–1713.
[16] Wang, L., Dai, H. L., and Han, Y. Y., 2012, "Cross-Flow-Induced Instability and Nonlinear Dynamics of Cylinder Arrays With Consideration of Initial Axial Load," Nonlinear Dyn., **67**(2), pp. 1043–1051.
[17] Price, S. J., and Paidoussis, M. P., 1984, "An Improved Mathematical Model for the Stability of Cylinder Rows Subject to Cross-Flow," J. Sound Vib., **97**(4), pp. 615–640.
[18] Granger, S., and Paidoussis, M., 1996, "An Improvement to the Quasi-Steady Model With Application to Cross-Flow-Induced Vibration of Tube Arrays," J. Fluid Mech., **320**(1), pp. 163–184.
[19] Li, H., and Mureithi, N., 2017, "Development of a Time Delay Formulation for Fluidelastic Instability Model," J. Fluids Struct., **70**, pp. 346–359.
[20] Mahon, J., and Meskell, C., 2013, "Estimation of the Time Delay Associated With Damping Controlled Fluidelastic Instability in a Normal Triangular Tube Array," ASME J. Pressure Vessel Technol., **135**(3), p. 030903.
[21] Sawadogo, T., and Mureithi, N., 2014, "Fluidelastic Instability Study on a Rotated Triangular Tube Array Subject to Two-Phase Cross-Flow—Part II: Experimental Tests and Comparison With Theoretical Results," J. Fluids Struct., **49**, pp. 16–28.
[22] Sandström, S., 1987, "Vibration Analysis of a Heat Exchanger Tube Row With ADINA," Comput. Struct., **26**(1–2), pp. 297–305.
[23] Azizian, R., and Mureithi, N., 2014, "A Simple Empirical Model for Tube–Support Normal Impact Interaction," ASME J. Pressure Vessel Technol., **136**(5), p. 051303.
[24] Saffarian, M. R., Fazelpour, F., and Sham, M., 2019, "Numerical Study of Shell and Tube Heat Exchanger With Different Cross-Section Tubes and Combined Tubes," Int. J. Energy Environ. Eng., **10**(1), pp. 33–46.
[25] Wahi, P., and Chatterjee, A., 2005, "Galerkin Projections for Delay Differential Equations," ASME J. Dyn. Syst. Meas. Control, **127**(1), pp. 80–87.
[26] Vyasarayani, C. P., Subhash, S., and Kalmár-Nagy, T., 2014, "Spectral Approximations for Characteristic Roots of Delay Differential Equations," Int. J. Dyn. Control, **2**(2), pp. 126–132.
[27] Das, S. L., and Chatterjee, A., 2002, "Multiple Scales Without Center Manifold Reductions for Delay Differential Equations Near Hopf Bifurcations," Nonlinear Dyn., **30**(4), pp. 323–335.
[28] Yi, S., Nelson, P. W., and Ulsoy, A. G., 2010, *Time-Delay Systems: Analysis and Control Using the Lambert W Function*, World Scientific, Hackensack, NJ.
[29] Asl, F. M., and Ulsoy, A. G., 2003, "Analysis of a System of Linear Delay Differential Equations," J. Dyn. Syst. Meas. Control, **125**(2), pp. 215–223.
[30] Jarlebring, E., and Damm, T., 2007, "The Lambert W Function and the Spectrum of Some Multidimensional Time-Delay Systems," Automatica, **43**(12), pp. 2124–2128.
[31] Yi, S., Nelson, P. W., and Ulsoy, A. G., 2007, "Survey on Analysis of Time Delayed Systems Via the Lambert W Function," Advances in Dynamical Systems, **14**(S2), pp. 296–301.
[32] Wahi, P., and Chatterjee, A., 2005, "Asymptotics for the Characteristic Roots of Delayed Dynamic Systems," ASME J. Appl. Mech., **72**(4), pp. 475–483.
[33] Vyasarayani, C. P., 2012, "Galerkin Approximations for Higher Order Delay Differential Equations," ASME J. Comput. Nonlinear Dyn., **7**(3), p. 031004.
[34] Sadath, A., and Vyasarayani, C. P., 2015, "Galerkin Approximations for Stability of Delay Differential Equations With Distributed Delays," ASME J. Comput. Nonlinear Dyn., **10**(6), p. 061024.
[35] Insperger, T., and Stépán, G., 2011, *Semi-Discretization for Time-Delay Systems: Stability and Engineering Applications*, Vol. 178, Springer Science & Business Media, New York.
[36] Butcher, E. A., Ma, H., Bueler, E., Averina, V., and Szabo, Z., 2004, "Stability of Linear Time-Periodic Delay-Differential Equations Via Chebyshev Polynomials," Int. J. Numer. Methods Eng., **59**(7), pp. 895–922.
[37] Breda, D., Maset, S., and Vermiglio, R., 2005, "Pseudospectral Differencing Methods for Characteristic Roots of Delay Differential Equations," SIAM J. Sci. Comput., **27**(2), pp. 482–495.
[38] Wu, Z., and Michiels, W., 2012, "Reliably Computing All Characteristic Roots of Delay Differential Equations in a Given Right Half Plane Using a Spectral Method," J. Comput. Appl. Math., **236**(9), pp. 2499–2514.
[39] Sun, J.-Q., 2009, "A Method of Continuous Time Approximation of Delayed Dynamical Systems," Commun. Nonlinear Sci. Numer. Simul., **14**(4), pp. 998–1007.
[40] Song, B., and Sun, J.-Q., 2011, "Low pass Filter-Based Continuous-Time Approximation of Delayed Dynamical Systems," J. Vib. Control, **17**(8), pp. 1173–1183.
[41] Vyhlidal, T., and Zítek, P., 2009, "Mapping Based Algorithm for Large-Scale Computation of Quasi-Polynomial Zeros," IEEE Trans. Autom. Control, **54**(1), pp. 171–177.
[42] Olgac, N., and Sipahi, R., 2002, "An Exact Method for the Stability Analysis of Time-Delayed Linear Time-Invariant (LTI) Systems," IEEE Trans. Autom. Control, **47**(5), pp. 793–797.
[43] Pekař, L., and Gao, Q., 2018, "Spectrum Analysis of LTI Continuous-Time Systems With Constant Delays: A Literature Overview of Some Recent Results," IEEE Access, **6**, pp. 35457–35491.
[44] Wahi, P., and Chatterjee, A., 2004, "Averaging Oscillations With Small Fractional Damping and Delayed Terms," Nonlinear Dyn., **38**(1–4), pp. 3–22.
[45] Molnar, T. G., Insperger, T., and Stepan, G., 2019, "Closed-Form Estimations of the Bistable Region in Metal Cutting Via the Method of Averaging," Int. J. Non-Linear Mech., **112**, pp. 49–56.
[46] Kalmár-Nagy, T., Stépán, G., and Moon, F. C., 2001, "Subcritical Hopf Bifurcation in the Delay Equation Model for Machine Tool Vibrations," Nonlinear Dyn., **26**(2), pp. 121–142.
[47] Nayfeh, A. H., and Balachandran, B., 2008, *Applied Nonlinear Dynamics: Analytical, Computational, and Experimental Methods*, Wiley, Hoboken, NJ.